

Investigation of the Sensitivity of Searches for Charged Higgs Bosons with the ATLAS Detector at the HL-LHC

Carl Schaffer

Bachelorarbeit in Physik
angefertigt im Physikalischen Institut
vorgelegt der
Fakultät für Mathematik und Physik
der
Albert-Ludwigs-Universität
Freiburg

September 2014

Hiermit versichere ich, die eingereichte Bachelorarbeit selbständig verfasst und keine anderen als die von mir angegebenen Quellen und Hilfsmittel benutzt zu haben. Wörtlich oder inhaltlich verwendete Quellen wurden entsprechend den anerkannten Regeln wissenschaftlichen Arbeitens (lege artis) zitiert. Ich erkläre weiterhin, dass die vorliegende Arbeit noch nicht anderweitig als Bachelorarbeit eingereicht wurde.

Freiburg im Breisgau,

Datum

.....

Unterschrift

Gutachter: Prof. Dr. Markus Schumacher

Contents

1	Introduction	1
2	Theory	3
2.1	Standard Model of Particle Physics	3
2.2	MSSM	4
2.2.1	Charged Higgs Bosons in the MSSM	5
2.3	Background Processes	6
3	ATLAS and the LHC	9
3.1	The Large Hadron Collider	9
3.2	The ATLAS Experiment	10
3.2.1	Overview	10
3.2.2	ATLAS Coordinate System	11
3.2.3	Detection with ATLAS	12
4	Data and Simulation	15
4.1	Samples used for Analysis	15
4.2	Detector Simulation	18
5	Search for Charged Higgs Bosons at 14 TeV and High Luminosity	25
5.1	Event Selection	25
5.1.1	Expected Event Yields	31
5.2	Expected Significance	34
5.3	Search at lower Luminosities	36
5.4	Comparison of Sensitivities	36
5.5	Study of different Systematic Uncertainties	38
6	Optimization of Analysis	41
6.1	Mass dependent Optimization	41
7	Conclusion	53
A	Zusammenfassung	55
	Bibliography	57
	Acknowledgements	59

Introduction

The Standard Model of particle physics is the currently established way of describing fundamental interactions and particles. It is based on the unification of electromagnetic and weak interaction formulated in 1961, see [1–4]. The Higgs boson was a required and postulated component since 1964, due to discovery of massive gauge bosons calling for electroweak symmetry breaking [5–7].

After the discovery of a Higgs boson at the European Organisation for Nuclear and Particle Research (CERN¹) and extensive further analysis of this discovery, many questions remain open. There are numerous phenomena which can still not be explained with the current models. Hypotheses and alternative theories have been and will be formulated, presenting experimental physicists with ever new challenges.

One approach is the concept of supersymmetry (SUSY) postulating additional superpartners for the currently known particles. The theory on which this analysis is based, the Minimal Supersymmetric Standard Model (MSSM) is the minimal extension of the Standard Model, with “minimal” indicating that the model introduces the fewest additional fields. It includes a total of five Higgs bosons, two of which carry electromagnetic charge. The observation of such charged Higgs bosons would suggest evidence for physics beyond the standard model. Large portions of the MSSM parameter space lead to predictions compatible with the recent discovery at the LHC [8, 9]. Finding evidence that this or another extension of the Standard Model is realized in nature, is one of the main goals of the ATLAS experiment at the Large Hadron Collider (LHC). The intended goal of this analysis is to evaluate the sensitivity of the combination of the planned High-Luminosity Large Hadron Collider (HL-LHC) and an upgraded ATLAS detector to charged Higgs bosons decaying via $H^\pm \rightarrow (\tau^\pm + \nu_\tau)$. Research so far has excluded the existence of charged Higgs bosons at masses below the top quark mass, which is why this analysis will concentrate on determining possible future improvement for already existing limits in the mass range from 200 GeV to 600 GeV in a data set corresponding to an integrated luminosity of 3000 fb⁻¹. Because currently only assumptions and extrapolations of data-taking conditions and detector performance are available to quantify future data taking conditions, this study uses simulation data according to the projected performance evaluations conducted by the ATLAS collaboration [10, 11]. The starting point of the study is a previously performed search for charged Higgs bosons published in 2013, using data collected during Run 1 [12].

In the following chapters, the broader theoretical concepts relevant to this thesis are introduced, including, but not limited to, the Standard Model and its supersymmetric extension. As the study is

¹ Conseil Européen pour la Recherche Nucléaire

focused on the measurement capabilities of the ATLAS detector and the LHC, the detector and its functionality are introduced. Also, the LHC upgrade progress so far, as well as future plans, such as the HL-LHC scheduled to be operative around 2020, will be briefly summarized. A section introducing the methods and assumptions used to predict future performance of the ATLAS experiment is included.

After describing the event selection, the distributions of the remaining events are used to calculate the expected sensitivity towards charged Higgs bosons. As a model independent quantification, the limits on $\sigma \times \text{BR}(H^+ \rightarrow \tau\nu_\tau)$ of the charged Higgs boson production process are calculated. To estimate the model dependent predictions with the final state of the LHC, expected exclusion limits for the $\tan\beta - m_{H^+}$ plane of the MSSM $m_{H^+}^{\text{max}}$ scenario are determined. To provide an outlook to a nearer future (specifically during Run 3), an additional analysis with an integrated luminosity of 300 fb^{-1} is emulated. In order to exploit currently available and future data ideally, analysis parameters are optimized for different Higgs boson mass hypotheses. After these studies, a brief summary and assessment of the sensitivity that can be achieved with the expected luminosities is given.

Theory

2.1 Standard Model of Particle Physics

The Standard Model of particle physics as described in [1–4] is the result of many years of research and describes a wide variety of reactions between elementary or compound particles of small scale. It describes three generations of fermions (particles with half numbered spin $\pm\frac{1}{2}$), each containing two quarks and one charged lepton with its corresponding lepton-neutrino. The three sets have almost identical properties, the only distinction being the increasing mass of the particles in each generation. Atoms are comprised from particles consisting only of quarks and leptons of the first generation. A list of the particles and some of their properties can be found in Table 2.1.

Particle	Symbol	Mass	Electric Charge
1st Generation			
up-quark	u	$(2.3^{+0.7}_{-0.5})$ MeV	$+\frac{2}{3}$
down-quark	d	$(4.8^{+0.5}_{-0.3})$ MeV	$-\frac{1}{3}$
electron	e	0.511 MeV	-1
electron neutrino	ν_e	< 2 eV	0
2nd Generation			
charm-quark	c	(1.257 ± 0.025) GeV	$+\frac{2}{3}$
strange-quark	s	(95.0 ± 0.5) MeV	$-\frac{1}{3}$
muon	μ	105.65 MeV	-1
muon neutrino	ν_μ	< 0.19 MeV CL = 90.0%	0
3rd Generation			
top-quark	t	$(173.07 \pm 0.57$ (stat.) ± 0.72 (sys.)) GeV	$+\frac{2}{3}$
bottom-quark	b	(4.18 ± 0.03) GeV	$-\frac{1}{3}$
tau	τ	(1776.82 ± 0.16) MeV	-1
tau neutrino	ν_e	< 18.2 MeV CL = 95.0%	0

Table 2.1: Overview of all elementary fermions described by the Standard Model by generation. The masses given are taken from [13], electrical charge is in units of e , the elementary charge.

These particles interact by exchanging gauge bosons. There are, after taking into account the unification of electromagnetic and weak interactions, two fundamental ways to interact:

- The **Strong Interaction** is the interaction mode inherent to particles carrying color charge, namely quarks and gluons. The strong force is mediated by exchange of the massless “gluons”, which couple to and carry color charge. Particles with non-neutral color charge cannot exist as a stable state. Due to this fact, the effect of the strong force is only relevant for very short distances (confinement).
- The **Electroweak Interaction** is the unification of electromagnetic and weak interactions as proposed by Glashow, Weinberg and Salam [1, 3, 4]. Particles interact electromagnetically through exchange of “photons”. Photons are stable, massless, neutral particles, causing the electromagnetic interaction to have an infinite range as opposed to strong and weak forces. The weak interaction is mediated by a charged and a neutral current. The charged current corresponds to the exchange of W^+ and W^- bosons, while the neutral current is attributed to the Z^0 boson. The unification postulates, that both electromagnetic and weak forces are different components of a more general force. The gauge bosons that mediate the weak force are the only ones carrying mass, which leads to a strongly limited range for the weak interaction. An overview of the gauge bosons can be seen in Table: 2.2.

Particle	Associated Interaction	Mass	Charge [e]
g	strong	0	0
γ	electromagnetic	$< 1 \times 10^{-18}$ eV	0
W^\pm	weak, charged	(80.385 ± 0.015) GeV	± 1
Z^0	weak, neutral	(91.1876 ± 0.0021) GeV	0

Table 2.2: Overview of the properties of gauge bosons from [13]. Charge is given in units of the elementary charge.

The masses of the W^\pm , Z^0 bosons as well as fermion masses violate the local gauge invariance. This shows that a mechanism of electroweak symmetry breaking is required. For this purpose, the Higgs-field and the corresponding scalar potential is introduced, which includes a complex isospin doublet. With the unitary gauge, this leads to one Higgs boson and three Goldstone bosons yielding the longitudinal degrees of freedom for the W^\pm and Z^0 bosons. The Yukawa coupling allows for the Higgs boson to couple to fermions, explaining their masses [14].

2.2 MSSM

The Minimal Supersymmetric Standard Model (MSSM) is an extension of the well-established Standard Model described in 2.1. A “superpartner” for each Standard Model particle is postulated [15]. To prevent gauge anomalies, SUSY requires a second doublet of complex scalar fields. The longitudinal degrees of freedom provided by this extension are absorbed into the masses of the W^\pm and Z^0 bosons, which leaves five physical Higgs bosons for the MSSM Higgs sector. Two of these five bosons (H^\pm) carry electromagnetic charge. These particles will, be referred to as H^+ , the charge-conjugated particles/processes are always implied. One of these Higgs bosons is compatible with the recent discovery of a neutral Higgs boson at CERN [8, 9], while the properties of the others remain widely unknown apart from SUSY predictions regarding CP -behavior and mass relations between them. There are five postulated Higgs bosons in total, the CP -even h^0 and H^0 , the CP -odd A^0 and the two charged Higgs bosons H^+ and H^- . The popular interpretation matches the neutral Higgs boson recently discovered at CERN to the lighter neutral MSSM boson, the h^0 , but there are also theories interpreting it as the

heavy neutral boson H^0 . No evidence towards the existence of any of these additional bosons has been found so far.

2.2.1 Charged Higgs Bosons in the MSSM

In this part, the expected processes containing production and decay of charged Higgs bosons are described, the final state is shown and the signal is described. The studies conducted with data taken by the ATLAS experiment have excluded charged Higgs boson masses up to $m_{H^\pm} < 160$ GeV and have also placed limits on higher mass ranges. Up to date, analysis of the H^\pm has yielded the following results: If a charged Higgs boson exists in the mass range between 90 GeV and 160 GeV, the branching ratio for the production via $t \rightarrow bH^\pm$ is less than 0.24% - 2.1% (at 95% confidence level). For heavy bosons (“heavy” referencing the comparison to the top-quark), the production cross-section limits for Higgs boson masses above the top quark mass are set from 0.0017 pb - 0.9 pb (see [12]). The $m_{H^\pm}^{\max}$ -scenario, for which limits are calculated during the course of this analysis, is a subspace of the MSSM parameter space used to simplify MSSM analysis. It is limited to two free parameters: the mass of the charged Higgs bosons relevant to this analysis, and $\tan\beta$, with β the ratio of vacuum-expectation values.¹

Figure 2.1 shows the leading order Feynman diagrams for the production of heavy H^\pm . The complete proposed processes analyzed for this study, corresponding to these Feynman diagrams are:

$$g\bar{b} \rightarrow [\bar{t}][H^+] \rightarrow [q\bar{q}\bar{b}][\tau^+ + \nu_\tau] \quad (2.1)$$

$$gg \rightarrow [\bar{t}b][H^+] \rightarrow [(q\bar{q}\bar{b})b][\tau^+ + \nu_\tau] \quad (2.2)$$

The final states used for this analysis demand a hadronic decay for the tau produced by the decaying H^\pm . The t-quarks in the Feynman diagrams in Figure 2.1 are required to decay into a b-quark and two light quarks. As can be seen, both of final states include at least three quarks, at least one of which is a bottom quark and a tau-neutrino pair in their final states. These objects are required in the event selection in section 5.1.

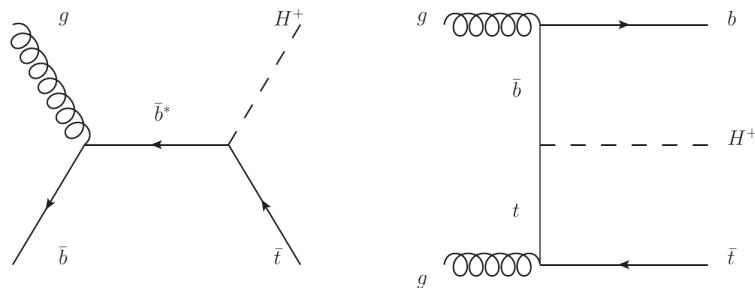


Figure 2.1: Example of leading-order Feynman diagrams for the production of charged Higgs bosons above the top quark mass. Figure taken from [12].

¹ The vacuum expectation values correspond to minima in the Higgs potential. The Value β is the ratio between the expectation values v_1 and v_2 for the supersymmetry Higgs doublet potential.

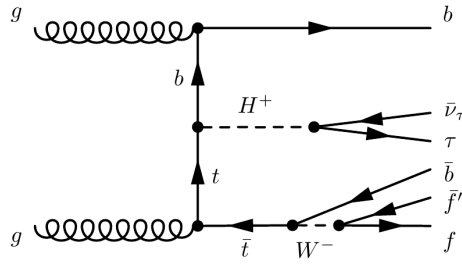


Figure 2.2: Example Feynman graph for charged Higgs boson production.

2.3 Background Processes

The term “background process” refers to processes likely to produce similar final states and kinematics to those of the desired signal process. For example replacing the H^+ boson in (Figure 2.2) with a W^+ boson results in a valid Feynman graph with the same final state and almost identical kinematics. Due to background processes and the small hypothetical cross section of the signal process, it is challenging to isolate signal events. In order to still be able to make meaningful statements concerning the existence of the sought after signal, the background processes are modeled as precisely as possible using established theoretical and experimental findings. An event selection is applied, discarding events with parameter regions expected or known to include vastly more background events than signal events.

Background processes which strongly differ from the signal, for instance those containing different particles in their final states can easily be suppressed. This class of events is referred to as reducible background. Other events that can falsely be identified as signal events are those where particles are misidentified. For instance if the W^\pm boson in the rightmost graph of Figure 2.7 decays into a $\tau\nu_\tau$ pair, the Z decays hadronically and a jet originating from a concurrent pp interaction is falsely included, the signature of this event can not be distinguished from a signal event. Similar misidentifications occur for the other background classes and, even though they are relatively rare, the large number of events in the background channels can lead to a significant amount of these errors in relation to the number of signal events.

For this analysis, the range of considered background event classes covers the production of single top quark events (Figure 2.3), the pair production of top quarks (Figure 2.4), the production of W^\pm bosons in association with jets (Figure 2.5), Z^0/γ^* production with associated jets (Figure 2.6) as well as di-boson events (Figure 2.7). An important background not considered in this study is multi-jet background. Due to its high cross section it is not viable to simulate this background, so it must be estimated from data. Since, so far, no data at $\sqrt{s} = 14$ TeV has been taken, this background can not be accounted for in this study. The cross sections for different background classes are included in Tables 4.2 and 4.2.

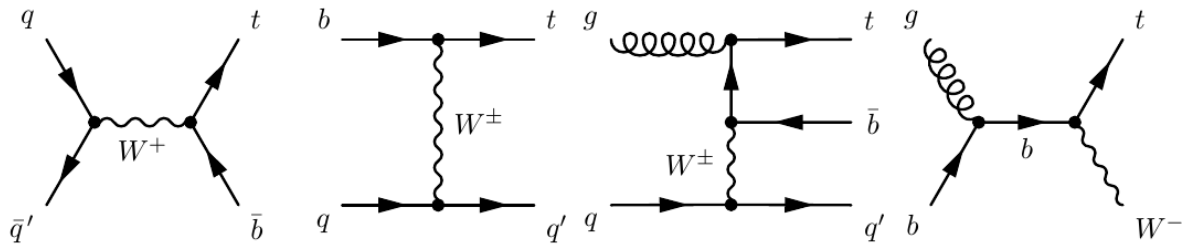


Figure 2.3: Dominant Feynman graphs for single top quark production [16].

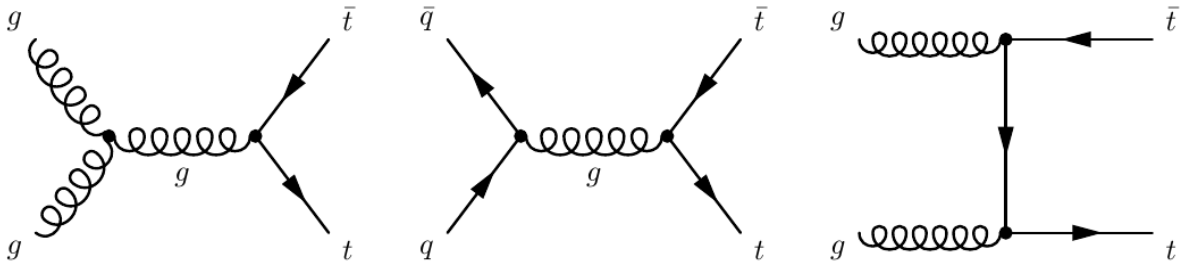


Figure 2.4: Leading order diagrams depicting pair production of top quarks [16].

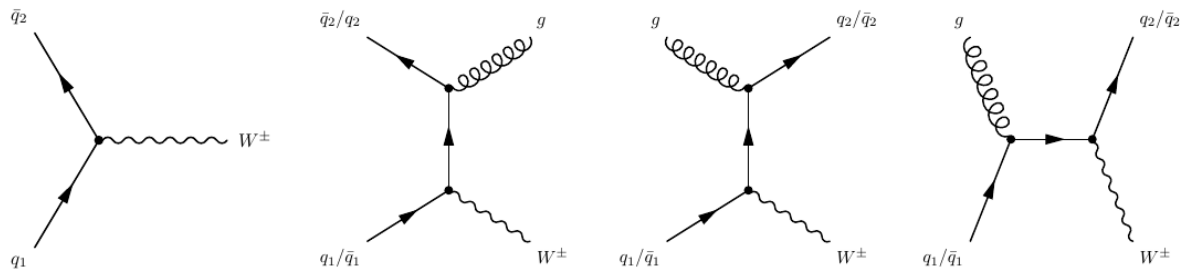


Figure 2.5: Feynman diagrams for the production of W^\pm bosons at leading order [17].

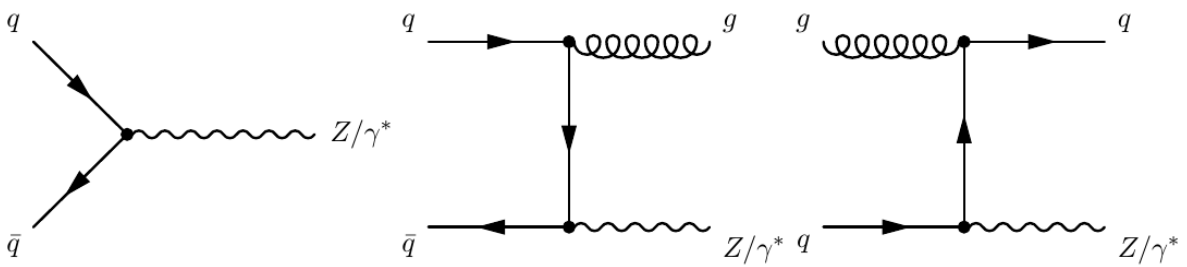


Figure 2.6: Dominant tree-level processes for Z/γ^* boson production [16].

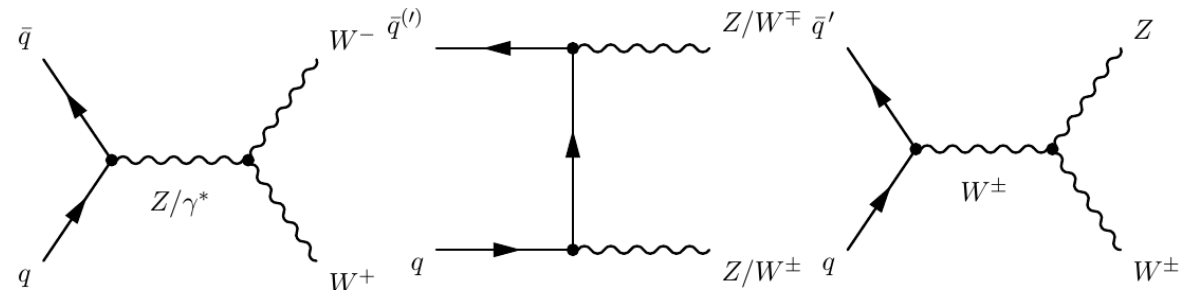


Figure 2.7: Feynman graphs showing dominant production modes for di-boson events [16].

ATLAS and the LHC

3.1 The Large Hadron Collider

The Large Hadron Collider (LHC), successor to the Large Electron Positron Collider is currently the world’s largest particle collider. It is located at the European Laboratory for Particle Physics CERN, near Geneva, Switzerland. It has been in operation since 2009, providing the particle collisions required to the four large experiments ATLAS¹, CMS², ALICE³ and LHCb⁴.

It is located in a circular tunnel of 27 km circumference up to 175 m below ground level. The LHC is the final link in a chain of successively more energetic accelerators. It hosts two beams of particles traversing the accelerator ring in opposite directions and collides them at four points in the ring. Each beam consists of about 3000 bunches, containing about 10×10^{10} protons each. The stability of their tracks is ensured using superconducting magnets cooled by liquid helium.

Currently the LHC can collide two beams of protons at 4 TeV each, resulting in a collision center-of-mass energy of $\sqrt{s} \approx 8$ TeV. Future plans for the LHC include a higher center-of-mass energy of up to 14 TeV and a reduced bunch spacing, resulting in higher instantaneous luminosities. A benchmark for the overall performance is the mean number of interactions per bunch crossing, $\langle\mu\rangle$. Currently the LHC provides around $\langle\mu\rangle = 20$ but there are predictions of values as high as $\langle\mu\rangle = 200$ (see Table 3.1) [10][11].

Date	Project	\sqrt{s} [TeV]	Expected Int. Luminosity [fb^{-1}]	Expected $\langle\mu\rangle$
2009-13	Run 1	up to 8	5 [pb^{-1}]	20
2015-17	Run 2	up to 13	75-100	25
2019-21	Run 3	up to 14	300	50-60
2024-30	HL-LHC	up to 14	3000	up to 200

Table 3.1: Upgrade process of the LHC from [10] and [11].

These high event rates are a vital part in collecting data of sufficient statistical impact for many analyses. The downside to high luminosities is, that as intervals between interactions decrease, uncer-

¹ A Toroidal LHC Apparatus

² Compact Muon Solenoid

³ A Large Ion Collider Experiment

⁴ Large Hadron Collider-beauty

tainties due to so called pileup⁵ events increase.

3.2 The ATLAS Experiment

The main goal of the ATLAS experiment is the verification of the Standard Model of particle physics and the examination of more advanced models. One major breakthrough achieved at the LHC in 2012 was the discovery of a neutral Higgs boson, which had been predicted since 1964 [5]. The ATLAS detector is a cylindrical detector of about 25 m of diameter, and a length of about 44 m. The particle beams provided by the LHC traverse the detector along its longitudinal axis and are brought to collision in the center of the detector. Particles produced in these collisions fan out in all directions and are registered by different detector subsystems along their path. A schematic of the detector can be seen in Figure 3.1.

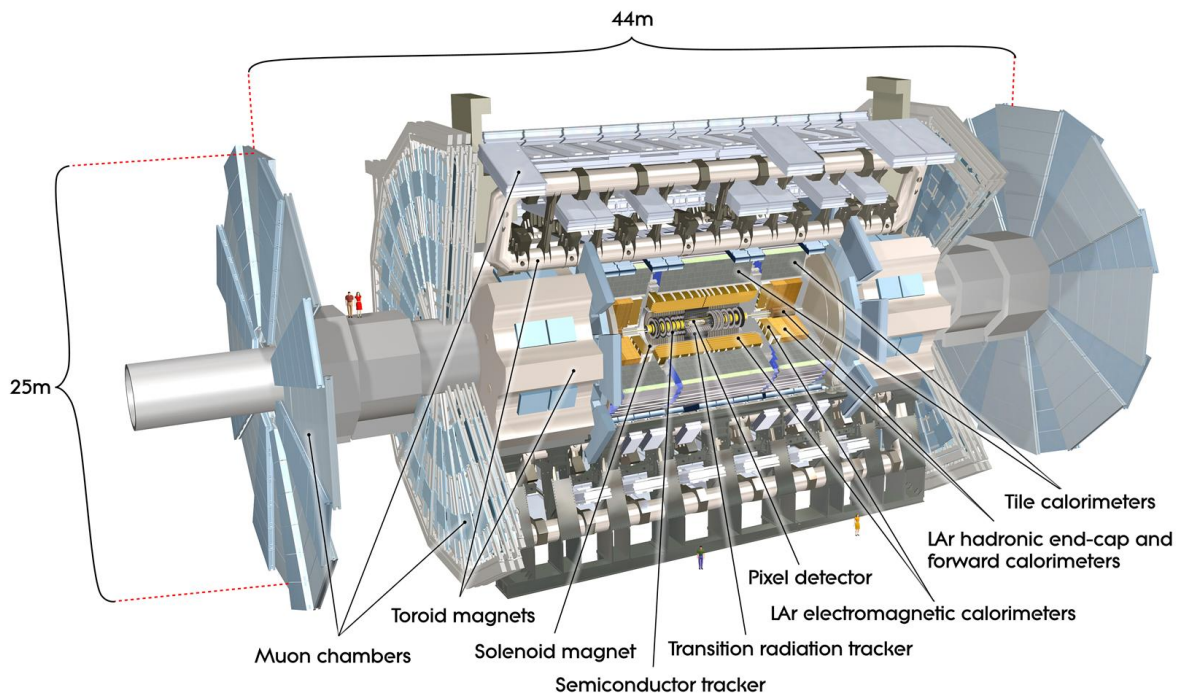


Figure 3.1: A schematic overview of the ATLAS Detector, showing a cut-away view. Taken from [18]

3.2.1 Overview

The detector consists of four main parts: The Inner Tracking Detector (ID), the electromagnetic calorimeter, hadronic calorimeter and the Muon Spectrometer (MS). Each component is optimized for the detection and measurement of certain types of particles, as will be elaborated on in section 3.2.3. The detector is separated into two main regions, the cylindrical barrel around the beam and the circle shaped endcaps.

⁵ Pileup describes the accumulation of particles in the detector. With the high luminosities new interactions occur and fresh waves of particles are produced while the detector is still processing previous events. This can lead to uncertainties regarding which interaction signatures should be assigned to, causing mixing of objects between different events.

The ID consists of high-resolution semiconductor pixel and strip detectors as well as the Transition Radiation Tracker. These components are designed to determine trajectories and vertices. Tracks can be reconstructed by analyzing the individual output of the very smallest detector components. Charged particles leave trails of ionized particles which can be observed as groups or individual deposits of energy in the inner detector. Pattern recognition algorithms perform the combination of these signals into tracks. Reconstruction and extrapolation of tracks allows precise reconstruction of primary and secondary vertices which are vital for flavor-tagging of jets. A strong magnetic field of about two Tesla, produced by a Solenoid magnet, causes curving tracks which can in turn be used to determine the transverse momentum of the charged initial particles.

Once particles leave the inner detector, they pass into the electromagnetic calorimeter, where electrons and photons are absorbed with a finely granular sampling calorimeter. The shape and total deposit of an electromagnetic shower can be used to identify some particle types and determine their initial energy. The hadronic calorimeter works in the same way, it measures the energy and location of incident particles by absorbing shower particles produced by the energy loss of the initial particle. The difference is, that the material used in the hadronic calorimeter is tailored towards absorbing particles interacting via strong interaction, thus absorbing all remaining particles apart from muons and neutrinos.

The outermost component of ATLAS is the Muon Spectrometer. It uses a strong magnetic field (ranging from 0.5 T in the central region to 1 T in the end cap regions [18]) in combination with Monitored Drift Tube Chambers and Cathode Strip Chambers to analyze muons.

Because the frequency of events occurring in the detector is significantly higher than the frequency at which events can be stored, a trigger system selects the events which are ultimately written to disk. The system consists of three main phases, the first of which is hardware based, using Muon Spectrometer and calorimetry data to preselect events with desired signatures. The data is piped into a buffer as a slower and more precise second trigger system reconstructs regions of interest. If an event passes this step, the whole event is reconstructed, representative parameters for the event are calculated and the final decision on whether to keep it is made. This procedure reduces the initial event frequency (order of magnitude 10×10^9 Hz) to a frequency that can be processed by equipment writing the final data. Ultimately a few hundred events are written to disk each second.

3.2.2 ATLAS Coordinate System

The coordinate system used for ATLAS is right-handed and defined in relation to the nominal interaction point (many quantities are also given in respect to the reconstructed primary vertex). The x -axis points towards the center of the LHC-ring, while the y -axis points straight upwards. The z -axis points tangential to the LHC ring, in a counterclockwise direction, when viewing the detector from above.

For describing particles and especially their trajectories in the detector, one uses spherical coordinates with respect to the nominal interaction point. Here, the azimuthal angle ϕ is measured in the plane fixed by the x -axis and the y -axis, the polar angle θ is measured from the positive z -axis. Instead of using the angle θ itself, one usually employs the so called “pseudorapidity” as defined in Eq. 3.1.

$$\eta = -\ln(\tan \theta/2) \quad (3.1)$$

Per construction, larger values of η are closer to the beam axis than smaller ones. This method of angular description holds several advantages, as differences in η are invariant to Lorentz-transformations and the produced particle density as a function of η is nearly constant.

Transverse Momentum and Missing Transverse Energy

The transverse momentum p_T is a central quantity in the description of LHC physics. It describes the momentum component of a particle, perpendicular to the beam axis. The reason why this value is so important is that there is an intrinsic knowledge of its distribution, we know that all initial particles contributing to the interactions in the detector carry exclusively momentum tangential to the z -axis. The missing transverse energy, E_T^{miss} , is determined by calculating the vectorial sum of all transverse momenta and inverting the direction of the resulting vector, ideally, if all particles are measured and correctly processed the resulting vector should vanish. This variable has larger statistical and systematic uncertainties compared to other possible variables, as it is produced by combining different objects reconstructed by several detector subsystems, making very precise selections in E_T^{miss} less viable.

3.2.3 Detection with ATLAS

For a precise physics analysis, it is vital to correctly identify the bulk of relevant physics objects. One method of ensuring the required precision is the triggering system mentioned above. In a first step, candidates for physics objects are reconstructed from detector data and identified according to different criteria. The following section shortly introduces methods used for particle identification. An overview of different particle signatures is shown in Figure 3.2.

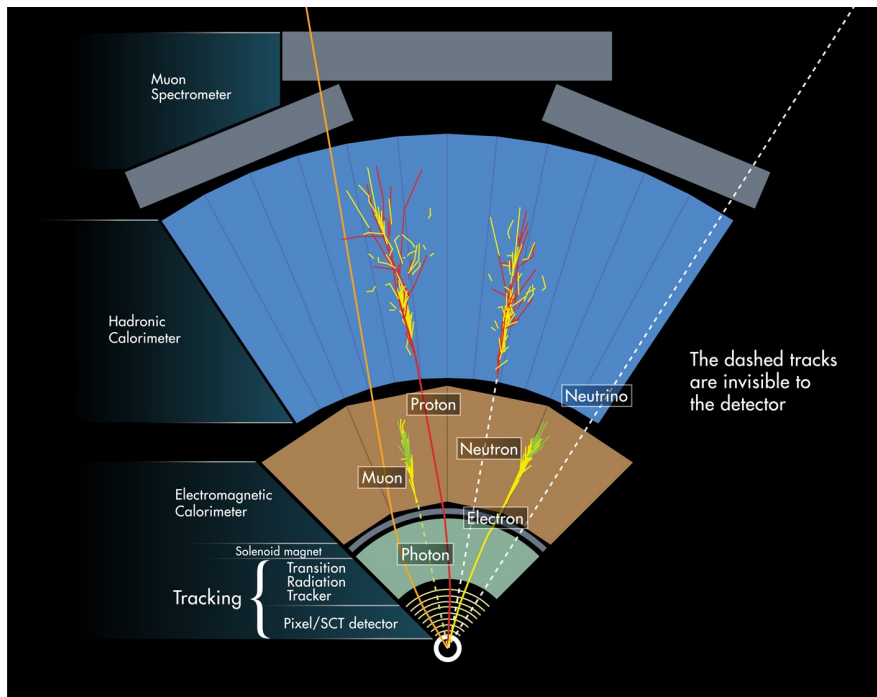


Figure 3.2: Schematic showing the detection of different particle types in the main ATLAS detector systems. The difference between electromagnetic and hadronic showers becomes apparent when comparing the calorimeter signatures of proton and neutron with those of electron or photon. Also, in the area of the Inner Detector the curving of the charged trajectories is visible.

The first main distinction is made between charged and neutral particles. Charged particles are far more easily detectable, as they interact with the detector via ionization, leaving observable tracks in

the inner detector. These tracks are curved due to the Lorentz-force exerted by the strong magnetic field produced by the solenoid. The momenta of these charged particles can be reconstructed from the curve of these tracks. The p_T -resolution $\left(\frac{\Delta p_T}{p_T}\right)$ is in general proportional to the absolute p_T , neglecting contributions from multiple scattering.

In the calorimeter all particles except for muons and neutrinos are absorbed. In the first section, the electromagnetic calorimeter, electrons and photons give rise to electromagnetic showers of nearly identical shape. The electrons however produce hits in the Inner Detector which can be reconstructed as a track, while photons, as neutral particles leave no such trace. The material of the electromagnetic calorimeter is such, that the particles primarily interacting electromagnetically are absorbed, while hadrons pass into the adjacent hadronic calorimeter. The HCAL is meant to completely absorb all hadrons, to ensure the total visible energy output to be measured. Distinctions between particles can again be made according to shape and energy of the observed deposit, as well as the charge information obtained from the Inner Detector. A special particle class are the neutrinos. They can not be observed by any of the detector systems, as their interaction probability is next to negligible. The presence of neutrinos can still be measured, as they carry energy and hence have a measurable effect on the overall event kinematics. Their presence is indicated by calculating the vector-sum of all observed particles. Ideally, this should return a zero-valued vector, if it does not, that is a strong indicator for neutrinos.

All of these systems are finely segmented in order to allow precise reconstruction of particle trajectories and shower shapes. The best granularity is attained for particles traveling perpendicular to the beam. Signatures can then be used to reconstruct physics object candidates and their properties. A more detailed explanation of identification criteria is included in Chapter 5.

Data and Simulation

Since this is a physics study for the High-Luminosity LHC, at the end of the planned runtime, with a total integrated luminosity of $L = 3000 \text{ fb}^{-1}$, only simulated data is available for analysis. As mentioned in Chapter 3, strong pileup effects are expected with values of $\langle\mu\rangle=140$ for Run 3 compared to $\langle\mu\rangle=20$ in Run 1, making improved measurement systems and methods necessary to maintain high precision in the busy detector environment. For most experimental aspects, it is assumed that the overall efficiency of the detector can be retained. This section explains the origin of the Monte Carlo samples used for analysis as well as the methods of the fast detector simulation that are applied. An overview of the data samples used in this study can be found in Tables 4.2 and 4.3. The cross sections for $\sqrt{s} = 14 \text{ TeV}$ were taken from [19–24]. An overview of the used generator software is included in Table 4.1.

4.1 Samples used for Analysis

Process		Generator
Signal		PowhegPythia
Single top	t - & Wt - channel	AcerMCPythia
	s -channel	PowhegPythia
$t\bar{t}$		McAtNloJimmy
di-boson		McAtNloJimmy
Z+Jets		AlpgeNJimmy
W+Jets		AlpgeNJimmy

Table 4.1: Overview of used Monte-Carlo event generators.

The used data sets are generated according to current knowledge using Monte Carlo methods. The initial data contains truth¹ level physics objects for each event. These objects could be used to simulate detector response, fully emulating the expected reaction of each component. Due to the large amounts of data required for the simulation of the 14 TeV setup and especially the HL-LHC luminosities, resource requirements for a full detector simulation are far to high. The large luminosity is required due

¹ The label "truth" describes data sets containing raw simulated particles. This data holds values corresponding directly to actual physics objects without any detection or measurement effects.

Process	σ [fb]	N_{gen}	$N_{\text{exp}}@ 3000 \text{ fb}^{-1}$	Event weight
$gb \rightarrow H^+ t m_{H^+} = 200 \text{ GeV}$	583.695	1531169	1751090	1.14363
$gb \rightarrow H^+ t m_{H^+} = 300 \text{ GeV}$	82.2836	674338	246851	0.366064
$gb \rightarrow H^+ t m_{H^+} = 400 \text{ GeV}$	24.9455	310419	74836.5	0.241082
$gb \rightarrow H^+ t m_{H^+} = 500 \text{ GeV}$	8.75033	155779	26251	0.168514
$gb \rightarrow H^+ t m_{H^+} = 600 \text{ GeV}$	3.69997	79439	11099.9	0.139729
$W^\pm W^\pm \rightarrow (e\nu_e + e\nu_e)$	1388.35	338792	4165050	12.2938
$W^\pm W^\pm \rightarrow (e\nu_e + \mu\nu_\mu)$	1390.52	339316	4171570	12.294
$W^\pm W^\pm \rightarrow (e\nu_e + \tau\nu_\tau)$	1394.14	340174	4182440	12.295
$W^\pm W^\pm \rightarrow (\mu\nu_\mu + e\nu_e)$	1393.01	339906	4179020	12.2946
$W^\pm W^\pm \rightarrow (\mu\nu_\mu + \mu\nu_\mu)$	1392.59	339790	4177780	12.2952
$W^\pm W^\pm \rightarrow (\mu\nu_\mu + \tau\nu_\tau)$	1392.7	339780	4178090	12.2965
$W^\pm W^\pm \rightarrow (\tau\nu_\tau + e\nu_e)$	1392.07	339732	4176220	12.2927
$W^\pm W^\pm \rightarrow (\tau\nu_\tau + \mu\nu_\mu)$	1392.8	339852	4178400	12.2948
$W^\pm W^\pm \rightarrow (\tau\nu_\tau + \tau\nu_\tau)$	1395.9	333806	4187710	12.5454
$W^\pm Z^0 + 0 \text{ jets}$	1940.96	500000	5822880	11.6458
$W^\pm Z^0 + 1 \text{ jets}$	1566.83	250000	4700490	18.8019
$W^\pm Z^0 + 2 \text{ jets}$	1057.25	150000	3171750	21.145
$W^\pm Z^0 + \geq 3 \text{ jets}$	832.105	100000	2496310	24.9631
$Z^0 Z^0 + 0 \text{ jets}$	1480.56	500000	4441670	8.88334
$Z^0 Z^0 + 1 \text{ jets}$	847.375	250000	2542130	10.1685
$Z^0 Z^0 + 2 \text{ jets}$	417.994	150000	1253980	8.35989
$Z^0 Z^0 + \geq 3 \text{ jets}$	255.044	100000	765131	7.65131
Single top t -Channel	78820	51465280	236460000	4.59455
Single top s -Channel	3904.19	12000000	11712600	0.976047
Single top Wt -Channel	84198.3	20000000	252595000	12.6297
$t\bar{t}$	531854	11362854	1595560	140.419

Table 4.2: Overview of samples used for analysis, with corresponding cross sections for $\sqrt{s} = 14 \text{ TeV}$, number of generated simulated events, expected number of events for an integrated luminosity of 3000 fb^{-1} as well as event weight used to scale histograms to number of expected events. Also see Table 4.3. The signal cross section correspond to a value of $\tan\beta=50$

Process	σ [fb]	N_{gen}	$N_{\text{exp}}@ 3000 \text{ fb}^{-1}$	Event weight
$W^\pm \rightarrow \tau\nu_\tau + bb + 0$ jets	3215.8	200000	9647390	48.237
$W^\pm \rightarrow \tau\nu_\tau + bb + 1$ jets	3782.85	95000	11348600	119.459
$W^\pm \rightarrow \tau\nu_\tau + bb + 2$ jets	2501.49	75000	7504460	100.06
$W^\pm \rightarrow \tau\nu_\tau + bb + \geq 3$ jets	1799.74	20000	5399230	269.962
$W^\pm \rightarrow \tau\nu_\tau + 0$ jets	17802200	4900000	53406700000	10899.3
$W^\pm \rightarrow \tau\nu_\tau + 1$ jets	4110420	1910000	12331300000	6456.16
$W^\pm \rightarrow \tau\nu_\tau + 2$ jets	1425810	847000	4277440000	5050.11
$W^\pm \rightarrow \tau\nu_\tau + \geq 3$ jets	463417	341000	1390250000	4076.98
$Z^0 \rightarrow (e^\pm + e^\mp) + bb + 0$ jets	26910.8	500000	80732300	161.465
$Z^0 \rightarrow (e^\pm + e^\mp) + bb + 1$ jets	11686	500000	35058000	70.1161
$Z^0 \rightarrow (e^\pm + e^\mp) + bb + \geq 2$ jets	4802.16	436000	14406500	33.0424
$Z^0 \rightarrow (\mu^\pm + \mu^\mp) + bb + 0$ jets	26933.9	500000	80801800	161.604
$Z^0 \rightarrow (\mu^\pm + \mu^\mp) + bb + 1$ jets	11684.1	500000	35052200	70.1044
$Z^0 \rightarrow (\mu^\pm + \mu^\mp) + bb + \geq 2$ jets	4799.72	436000	14399200	33.0256
$Z^0 \rightarrow (e^\pm + e^\mp) + 0$ jets	1593810	4880000	4781420000	979.8
$Z^0 \rightarrow (e^\pm + e^\mp) + 1$ jets	407931	1110000	1223790000	1102.52
$Z^0 \rightarrow (e^\pm + e^\mp) + 2$ jets	147974	745000	443921000	595.868
$Z^0 \rightarrow (e^\pm + e^\mp) + 3$ jets	49959	300000	149877000	499.59
$Z^0 \rightarrow (e^\pm + e^\mp) + 4$ jets	15912.5	118000	47737400	404.554
$Z^0 \rightarrow (e^\pm + e^\mp) + \geq 5$ jets	6140.63	36700	1.8421900	501.959
$Z^0 \rightarrow (\mu^\pm + \mu^\mp) + 0$ jets	159430	30000	4782890000	159430
$Z^0 \rightarrow (\mu^\pm + \mu^\mp) + 1$ jets	408151	1910000	1224450000	641.075
$Z^0 \rightarrow (\mu^\pm + \mu^\mp) + 2$ jets	147937	745000	443812000	595.72
$Z^0 \rightarrow (\mu^\pm + \mu^\mp) + 3$ jets	49904.1	300000	149712000	499.041
$Z^0 \rightarrow (\mu^\pm + \mu^\mp) + 4$ jets	15910	117000	47730100	407.949
$Z^0 \rightarrow (\mu^\pm + \mu^\mp) + \geq 5$ jets	6128.55	36900	18385600	498.256
$Z^0 \rightarrow (\tau^\pm + \tau^\mp) + 0$ jets	1593690	4900000	4781060000	975.726
$Z^0 \rightarrow (\tau^\pm + \tau^\mp) + 1$ jets	408053	1820000	1224160000	672.615
$Z^0 \rightarrow (\tau^\pm + \tau^\mp) + 2$ jets	147730	665000	443189000	666.45
$Z^0 \rightarrow (\tau^\pm + \tau^\mp) + 3$ jets	49856.5	300000	14957000	498.565
$Z^0 \rightarrow (\tau^\pm + \tau^\mp) + 4$ jets	15897.8	115000	47693500	414.726
$Z^0 \rightarrow (\tau^\pm + \tau^\mp) + \geq 5$ jets	6168.81	36800	18506400	502.892

Table 4.3: Overview of samples used for analysis, with corresponding cross sections for $\sqrt{s} = 14 \text{ TeV}$, number of generated simulated events, expected number of events for an integrated luminosity of 3000 fb^{-1} as well as event weight used to scale histograms to number of expected events. Also see Table 4.2

to the rareness of the process ($H^+ \rightarrow \tau\nu_\tau$) compared to the large background cross sections. To prevent this massive resource usage, the detector response is instead simulated with parametrisations of detector resolution and reconstruction efficiency, depending on truth particle properties. This procedure only uses a fraction of the resources required for full simulation while still retaining a reasonable level of credibility. The generated samples do not intrinsically contain the amount of events expected for the integrated luminosity of 3000 fb^{-1} . While they do contain a large amount of data, they are still only representative samples. The initially generated events are weighted to produce a distribution with the total sum of weights equal to the expected number of events, which leads to the behavior, that samples with relatively few simulated events (in respect to the corresponding cross-section) tend to model the shape of the expected distribution poorly, as single events are likely to have large weights. In our case, this is especially affects the W^\pm +jets and Z^0 +jets backgrounds, but as these background classes can be suppressed very well with the event selection as described in 5.1.1, a precise rendering of their shapes is nonessential. For this study, a total of about 130 million simulated truth level events is used.

4.2 Detector Simulation

The simulation of the detector consists of two large effects, the detector resolution and the reconstruction efficiency. Both of these effects are dependent on event-wide, particle specific or luminosity related quantities such as p_T , ΣE_T , η or $\langle\mu\rangle$. The modeling of the reconstruction efficiencies also includes a consideration of the probability of misidentifying objects (often labeled as "fake"), as well as considerations regarding the $|\eta|$ ranges covered by the detector. Resolution effects are modeled by fitting functions assumed to describe their behavior to available data and extrapolating towards the required parameter regions. The true values of the concerned properties are then modified using a random value from the corresponding resolution function. Reconstruction efficiencies are extrapolated likewise and objects are randomly discarded or misidentified according to corresponding parametrisations. In the following sections this will be elaborated, as the specific procedure varies depending on the objects. The particles required for this analysis are: jets, taus, muons, electrons and the missing transverse energy as well as the description of b-tagging efficiencies. The methods and values described here are taken from [10] and [11].

Muons

As muons are surveyed by the Inner Detector as well as the Muon Spectrometer, it is necessary to examine the resolution of both systems separately. The distinct functions for modeling the momentum resolution of both components are:

$$\sigma_{\text{ID}} = p_T \cdot \sqrt{a_1^2 + (a_2 \cdot p_T)^2} \quad (4.1)$$

$$\sigma_{\text{MS}} = p_T \cdot \sqrt{\left(\frac{b_0}{p_T}\right)^2 + b_1 + (b_2 \cdot p_T)^2} \quad (4.2)$$

$$(4.3)$$

this results in a combined resolution of:

$$\sigma_{\text{combined}} = \frac{\sigma_{\text{ID}} \cdot \sigma_{\text{ms}}}{\sqrt{\sigma_{\text{ID}}^2 + \sigma_{\text{ms}}^2}} \quad (4.4)$$

where p_T is the truth muon transverse momentum. The parameters a_1 and a_2 as well as b_0 , b_1 and b_2 were determined using the Run 1 MS setup. It is assumed, that they will still be valid for coming experiments. The absolute values of the parameters used can be found in Table 4.4

η range		a1	a2	
0.00	0.18	0.01061	0.000157	
1.80	0.36	0.01084	0.000153	
0.36	0.54	0.11240	0.000150	
0.54	0.72	0.01173	0.000149	
0.72	0.90	0.01269	0.000148	
0.90	1.08	0.01406	0.000161	
1.08	1.26	0.01623	0.000192	
1.26	1.44	0.01755	0.000199	
1.44	1.62	0.01997	0.000232	
1.62	1.80	0.24530	0.000261	
1.80	1.98	0.31210	0.000297	
1.98	2.16	0.03858	0.037500	
2.16	2.34	0.05273	0.000465	
2.34	2.52	0.53290	0.000642	
2.52	2.70	0.05683	0.000746	
η range		b0	b1	b2
<	1.05	0.24	0.2676	0.0001
>	1.05	0.00	0.388	0.0001

Table 4.4: Parameters used for the parametrization of the muon p_T resolution. Adapted from [11].

The trigger and reconstruction efficiencies are also dependent on the detector regions traversed by the muons. The assumed efficiencies for different $|\eta|$ ranges are summarized in Table: 4.5

η	0:0.1	0.1:1.05	1.05:2.4	2.4:2.5	2.5:2.7
Reco. Tight	0.54	0.97			0.00
Trigger	0.70		0.86	0.00	

Table 4.5: Muon reconstruction and trigger efficiencies depending on η . The label "Tight" signifies selection criteria optimized towards data precision rather than reconstruction yield.

Missing transverse energy

The final value for the missing transverse energy E_T^{miss} is calculated from separately determined x and y components calculated as:

$$E_{x,y}^{\text{miss}} = E_{x,y}^{\text{miss,true}} + \text{Gaussian}(0, \sigma(\mu)) \quad (4.5)$$

The respective resolution of the missing transverse energy components depends on pileup and detector geometry. The parametrisation for $\sigma(\mu)$ has been determined in [10] using simulated samples for 14 TeV and values of $\langle\mu\rangle = (60, 80, 140)$. Another factor that influences the resolution of the energy is the total sum of transverse energy (ΣE_T) which is also evaluated in [10]. The total results for ΣE_T -dependencies are adopted from [10] and are included in Figure 4.1. scope of this study.

Jets

Jet p_T resolution is parametrized by:

$$\sigma_{p_T} = \sqrt{\frac{N^2}{p_T^2} + \frac{S^2}{p_T} + C^2} \quad (4.6)$$

where N is a noise-dependent linear function of μ :

$$N(\mu) = a(\eta) + b(\eta) \cdot \mu \quad (4.7)$$

S is estimated according to stochastic considerations and C is assumed to remain constant. Values for the used parameters can be found in Table 4.6. The detector simulation uses distinct parameters for different detector regions, differentiating between barrel, extended barrel, endcap and the forward detector (which explains the η dependency in 4.7). Jet reconstruction efficiency is extrapolated from data at $\langle\mu\rangle=20-40$ to the p_T dependent values included in Table 4.7. Jet reconstruction performance increases significantly with jet p_T .

η range		a	b	S	C
0.00	0.80	3.2	0.07	0.74	0.05
0.80	1.20	3.0	0.07	0.81	0.05
1.20	2.80	3.3	0.08	0.54	0.05
2.80	3.60	2.8	0.11	0.83	0.05

Table 4.6: Parameters for Jet p_T resolution used in Equations 4.6 and 4.7.

Jet p_T	ϵ
20-30 [GeV]	75%
30-35 [GeV]	80%
50 [GeV]	> 95%

Table 4.7: Jet reconstruction efficiency as described in [11]. Reconstruction efficiency are assumed to improve with transverse momentum.

b-Tagging

b-Jets are distinguished using two separate algorithms, the combined 3D track impact parameter as well as the multivariate tracker MV algorithm described in Ref. [25]. The performance is parametrized as a function of η and p_T . The results obtained in [10] are included in Figure 4.2. The mistagging probabilities describing the amount of other jets that are tagged as b-jets are included in Figure 4.3.

The average efficiency corresponding to the working point used is about 70% corresponding to a relative light jet rejection rate of 50% for $\langle\mu\rangle=140$ and about 75% for $\langle\mu\rangle=60$.

Electrons

Electron detection will become significantly harder with the increasing luminosities which cause an increase in the probability of reconstructing fake electrons due to pileup. For this reason, new methods using multivariate criteria are currently in development. It is assumed that in this way the current performance levels can be held in future analysis. The assumed efficiency parametrizations used are

$$\epsilon(p_T) = 0.85 - 0.191 \cdot \exp^{1-\frac{p_T}{20}} \quad (4.8)$$

for correct identification of real electrons and

$$\epsilon(p_T) = 0.0018 \cdot \exp^{-0.035 \cdot p_T} \quad (4.9)$$

to parametrize the misidentification probability of jets as electrons. As for muons, reconstruction of electrons is conducted using "tight" criteria. The future energy resolution is assumed to be consistent with the currently used parametrization of:

$$\sigma(GeV) = 0.3 \oplus 0.10 \cdot \sqrt{E(GeV)} \oplus 0.010 \cdot E(GeV) \text{ for } |\eta| < 1.4, \quad (4.10)$$

$$\sigma(GeV) = 0.3 \oplus 0.15 \cdot \sqrt{E(GeV)} \oplus 0.015 \cdot E(GeV) \text{ for } 1.4 < |\eta| < 2.47 \quad (4.11)$$

Where the operator \oplus signifies quadratic addition $a \oplus b = \sqrt{a^2 + b^2}$.

Tau Leptons

Tau leptons exhibit two different possible decay paths, each requiring different detection methods. They have a probability of approximately one third to decay leptonically and about two thirds for hadronic decay. Leptonic tau decays cannot be distinguished from prompt lepton production in our analysis, and for this reason they are not considered here.

Detection of hadronically decaying taus is modeled according to the assumption that the performance observed in recent data and Monte Carlo studies can be retained for higher pileup-samples. In the past the reconstruction efficiency has remained stable against increases in pileup and number of vertices. The efficiencies assumed are included in Figure 4.4. The relevant graph in this figure is the one corresponding to the tight criteria, showing an average efficiency of roughly 40% for both one and three prong hadronic decays. These values are relatively low, because the strong signature similarity between jets seeded by quarks and those produced by tau leptons necessitates strict identification criteria in order to achieve the required high purity. The energy resolution for hadronically decaying taus depending on the charged multiplicity of the decay is given by:

$$\sigma(GeV) = 0.3 \oplus \left(0.62 / \sqrt{E(GeV)}\right) \text{ for one prong} \quad (4.12)$$

$$\sigma(GeV) = 0.3 \oplus \left(0.76 / \sqrt{E(GeV)}\right) \text{ for three prongs} \quad (4.13)$$

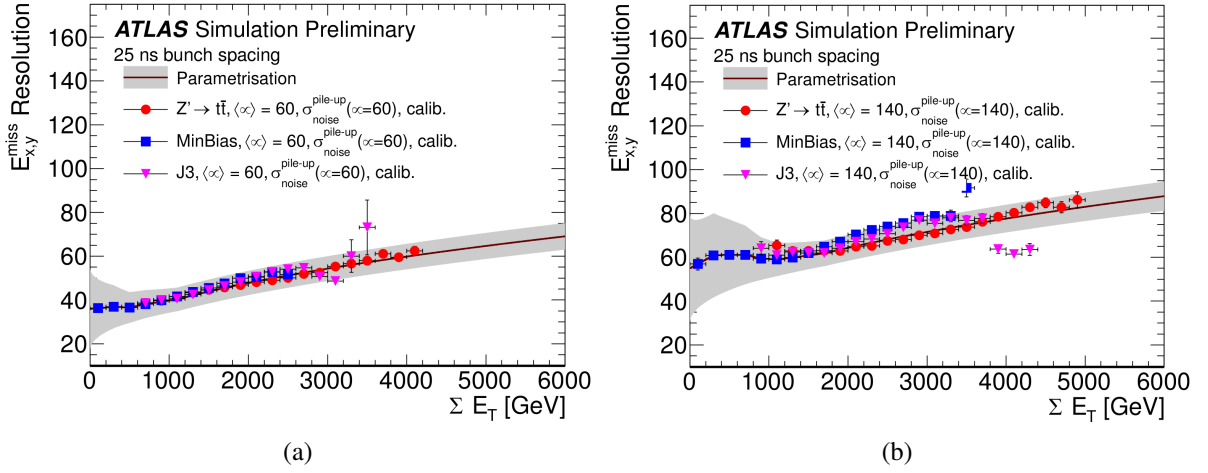


Figure 4.1: The resolution of missing transverse energy in dependency of the total transverse energy. Figure (a) represents a mean number of interactions of $\langle\mu\rangle=60$. Figure (b) corresponds to $\langle\mu\rangle=140$. The different graphs correspond to different sets of data used for determining the parametrization, which is shown as a line with the corresponding error bands. The figures are adopted from [10].

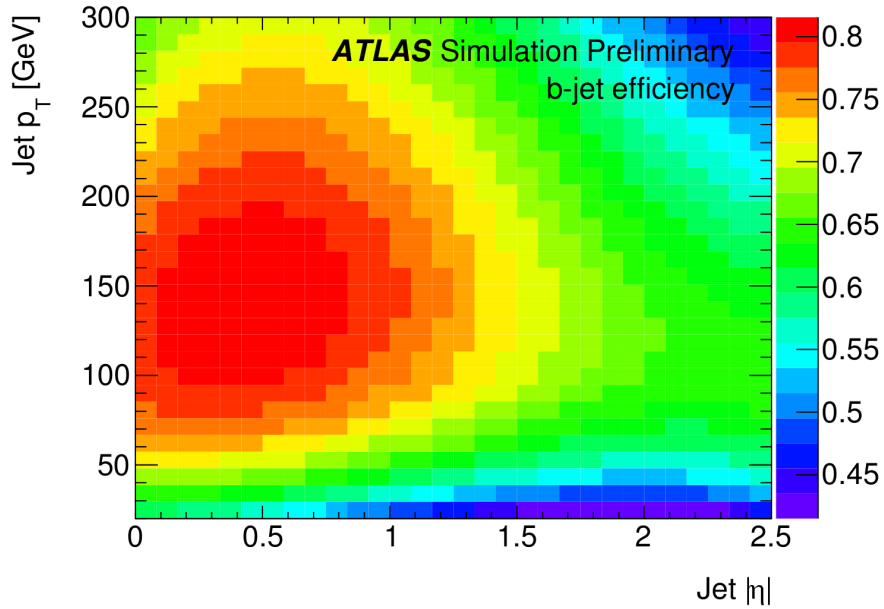


Figure 4.2: Efficiency of b-tagging depending on the transverse momentum and pseudorapidity for jets originating in b-Quarks [10].

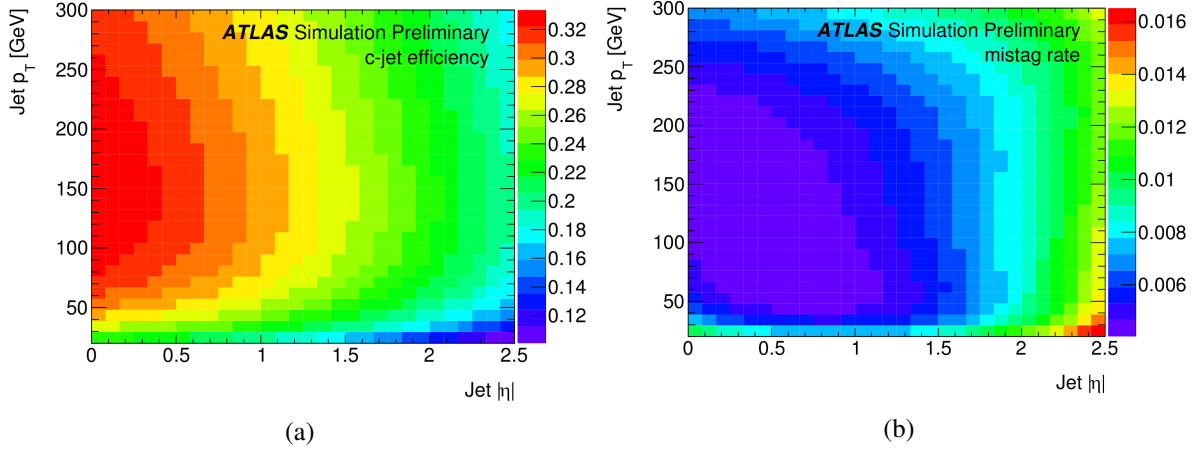


Figure 4.3: Probability of jets being misidentified as a function of the transverse momentum and the pseudorapidity of the initial jet. (a) shows the mistag probability for c-Jets, figure (b) describes the mistag rate for jets originating from lighter quarks [10].

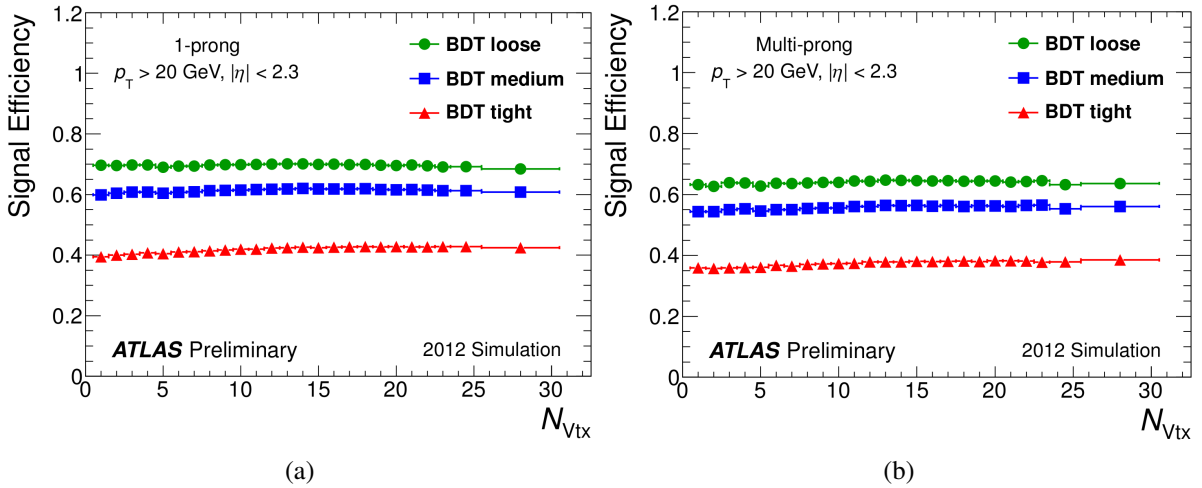


Figure 4.4: Reconstruction efficiencies of hadronically decaying tau leptons. The left figure describes tau decays with one charged track, the left one for three tracks. The relevant graphs are those corresponding to the "tight" criteria [11].

Search for Charged Higgs Bosons at 14 TeV and High Luminosity

This chapter describes the main component of this study, the determination of the expected sensitivity of a fully upgraded ATLAS detector and the HL-LHC with an expected integrated luminosity of 3000 fb^{-1} towards heavy charged Higgs bosons. It also describes a modification of this analysis used to estimate the prospects for the search during Run 3 with an integrated luminosity of 300 fb^{-1} . After a general introduction of the analysis concept as the first part of this chapter, the applied event selection is motivated and discussed in detail. The expected sensitivities for both Run 3 and Run 4 are estimated and compared to each other as well as to the results obtained in [12]. An additional section describes a study of the systematic uncertainties treated in [12] and their impact and implementation in this analysis.

General concept behind applied analysis

As already mentioned, this study utilizes data simulated for future data taking conditions to evaluate the expected sensitivity towards charged Higgs bosons. The study consists of three large parts, the first of which is the simulation of detector capabilities as discussed in Chapter 4.2. After this, an event selection is performed in order to select only events corresponding to final states of the signal as discussed in Section 2.2.1. This step also includes kinematic cuts designed to reduce specific background contributions. The third step is the evaluation of distribution of a discriminant for the final set of events provided by the event selection. This includes the calculation of limits on $\sigma_{H^+} \times \text{BR}(H^+ \rightarrow \tau + \nu_\tau)$ as well as using these limits to calculate parameter regions in the m_{H^+} vs $\tan\beta$ plane of the $m_{H^+}^{\text{max}}$ scenario that can be excluded.

5.1 Event Selection

The general idea behind the event selection process described in this section is to improve the overall signal to background ratio by selecting subsequent subsets of events that exhibit properties characteristic for the signal. It is a trade off between improving the signal to background ratio allowing better distinction and maintaining a good signal efficiency, which leads to lower statistical uncertainties. Also overly strict event selection can significantly alter the shape of variable distributions, causing

problems in later parts of the analysis while too loose selection does not sufficiently extract the signal for use in further analysis.

The applied cuts are listed in Table 5.1 and the expected distributions of the corresponding variables are included in Figures 5.1 to 5.6. The distributions in these figures are scaled to represent the total number of expected events for an integrated luminosity of 3000 fb^{-1} . The scaling factor applied to each histogram is calculated as

$$A = \frac{\sigma}{N_{\text{gen.}}} \cdot L \quad (5.1)$$

with σ denoting the cross section of the corresponding process, N_{gen} corresponding to the total number of generated events and the integrated luminosity L . A discussion of all applied cuts and corresponding expected event yields can be found on the following pages.

Cut #	Variable	Requirement
1	Number of Jets	≥ 3
2	Number of b-tagged Jets	≥ 1
3	Number of Taus with $p_T \geq 40 \text{ GeV}$	exactly 1
4	Number of reconstructed Leptons	exactly 1
5	Missing transverse Energy	$\geq 80 \text{ GeV}$
6	Transverse Energy Significance	≥ 12

Table 5.1: Overview of applied cuts of the baseline analysis

Number of Jets

For the search for charged Higgs bosons decaying as seen in the decay channels described in Equation 2.1, final states with a minimum of three identified jets are selected. This corresponds to the minimum amount of jets contained in the final state of the signal processes.

Number of b-Jets

As all expected signal final states also contain b quarks, inherent to the H^+ production process. Only events containing at least one b-jet are selected.

Transverse momentum of leading Tau Lepton Candidate

A lower threshold on the transverse momentum of the leading (most energetic) tau lepton is applied. This is due to the fact that taus with a lower energy are unlikely to originate from the decaying H^+ . The requirement is to have exactly one tau lepton with a p_T larger than 40 GeV, which corresponds to a cut in p_T and a subsequent one requiring exactly one tau lepton.

Number of Leptons

All events containing reconstructed leptons apart from the taus required by the previous cut are removed in this cut, as the considered final state does not contain additional leptons. This means that in the corresponding distributions in Figure 5.4 only events contained in the bin corresponding to exactly one reconstructed lepton (the tau from the previous cut) are selected.

Missing Transverse Energy

The missing transverse energy is an indicator for neutrino activity (as discussed in Section 3.2.3). As this study searches for H^+ decaying to $\tau + \nu_\tau$, at least one neutrino is present in the final state. Because neutrinos can not be directly measured, a missing transverse energy of at least 80 GeV is required.

Missing Transverse Energy Significance

The final requirement used for selecting events is $E_T^{\text{sign.}} > 12$ with $E_T^{\text{sign.}}$ defined as:

$$E_T^{\text{sign.}} = \frac{E_T^{\text{miss}}}{0.5 \cdot \sqrt{\sum p_T^{\text{PV}}}} \quad (5.2)$$

where E_T^{miss} is the missing transverse energy and $\sum p_T^{\text{PV}}$ describes the sum over the transverse momenta of all physics objects attributed to the primary vertex. This variable is similar to a significance of E_T^{miss} because the the resolution $\left(\frac{\sigma_{\text{emt}}}{E_T^{\text{miss}}}\right)$ scales with p_T sum. As the simulated data does not include tracking or vertex information, the exact reproduction of this variable is impossible. The approximation used instead is to take the scalar p_T sum over all identified jets and visible τ leptons instead. As the cut targets the suppression of multi-jet background, which is not considered in this analysis anyway, this different definition of the observable should not significantly change conclusions.

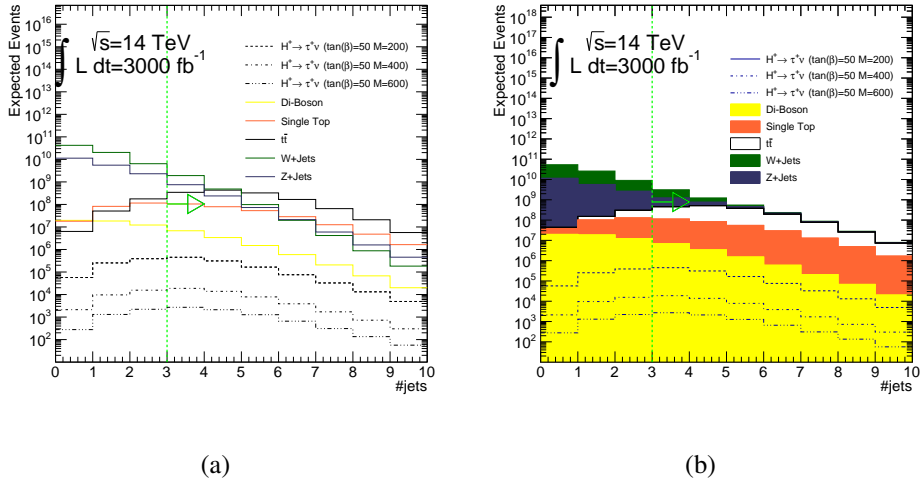


Figure 5.1: Distribution of the number of jets before N_{jet} event selection. Figure (a) superimposes all background histograms as well as three signal histograms for different m_{H^-} values. All histograms are scaled corresponding to their expected cross-sections.

Figure (b) shows the all background process histograms stacked, with the three signal histograms (again scaled according to expected cross-section) superimposed. A vertical line shows the applied event selection, an arrow indicates the part of the distribution that is kept.

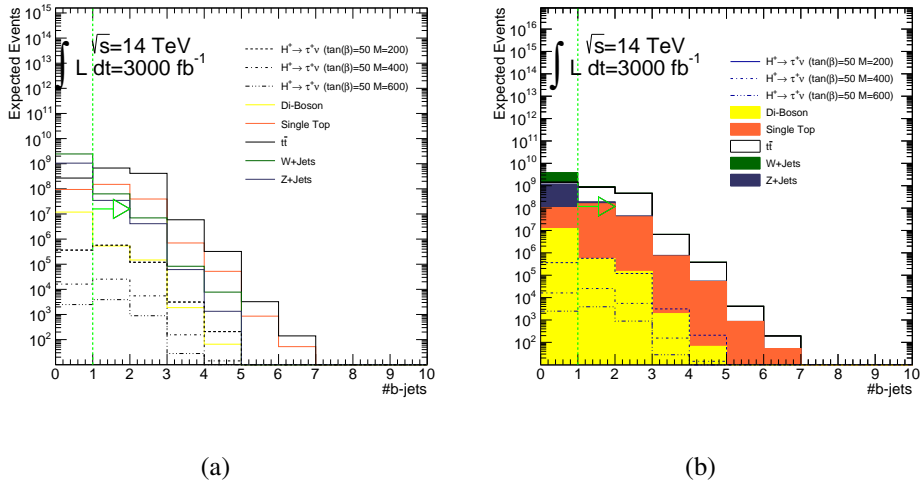


Figure 5.2: Distribution of the number of b-tagged jets before $N_{\text{b-jet}}$ event selection. Figure (a) superimposes all background histograms as well as three signal histograms for different m_{H^-} values. All histograms are scaled corresponding to their expected cross-sections.

Figure (b) shows all background process histograms stacked, with the three signal histograms (again scaled according to expected cross-section) superimposed. A vertical line shows the applied event selection, an arrow indicates the part of the distribution that is kept.

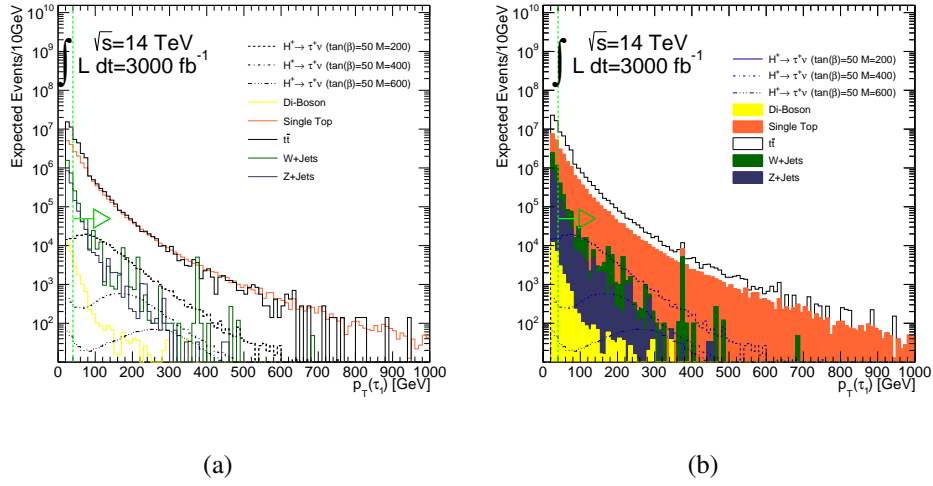


Figure 5.3: Distribution of the p_T of the leading tau lepton before the corresponding event selection step. Figure (a) superimposes all background histograms as well as three signal histograms for the different m_{H^+} values. All histograms are scaled corresponding to their expected cross-sections. Figure (b) shows all background process histograms stacked, with the three signal histograms (again scaled according to expected cross-section) superimposed.

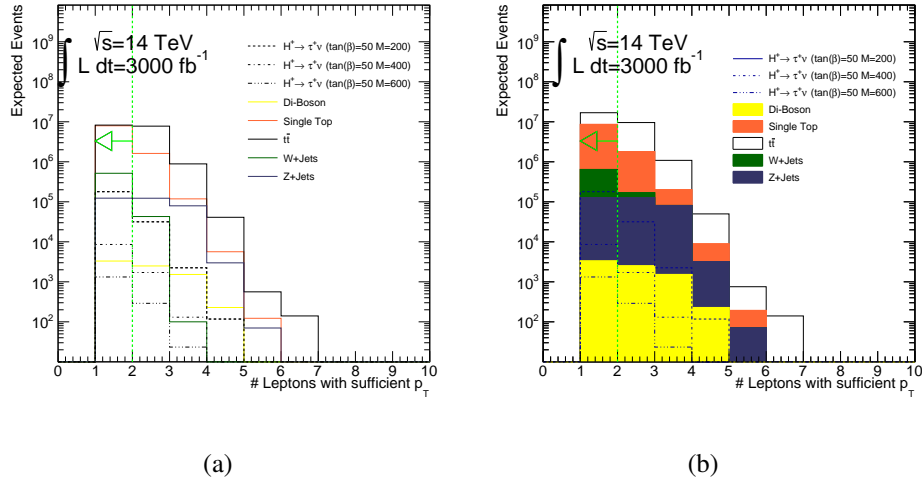


Figure 5.4: Distribution of the total number of leptons (including the tau lepton required in the previous cut) before the corresponding event selection step. Figure (a) superimposes all background histograms as well as three signal histograms for different m_{H^+} values. All histograms are scaled corresponding to their expected cross-sections. Figure (b) shows all background process histograms stacked, with the three signal histograms (again scaled according to expected cross-section) superimposed. A vertical line shows the applied event selection, an arrow indicates the part of the distribution that is kept.

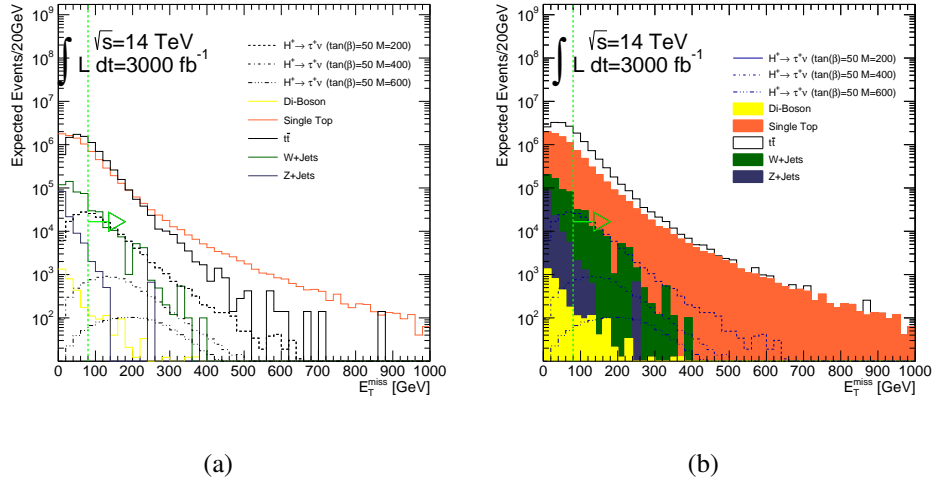


Figure 5.5: Distribution of the missing transverse energy before the corresponding event selection step. Figure (a) superimposes all background histograms as well as three signal histograms for different m_{H^\pm} values. All histograms are scaled corresponding to their expected cross-sections. Figure (b) shows all background process histograms stacked, with the three signal histograms (again scaled according to expected cross-section) superimposed. A vertical line shows the applied event selection, an arrow indicates the part of the distribution that is kept.

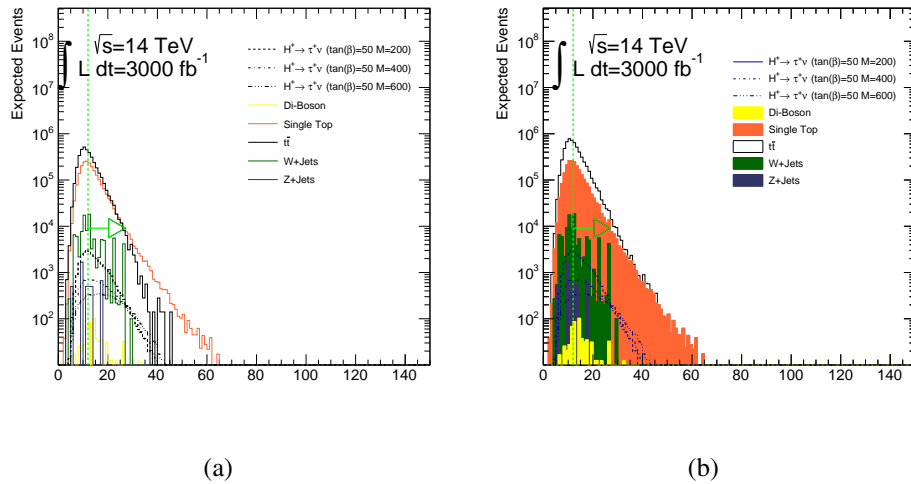


Figure 5.6: Distribution of $E_T^{\text{sign.}}$ before the corresponding event selection step. Figure (a) superimposes all background histograms as well as three signal histograms for different m_{H^\pm} values. All histograms are scaled corresponding to their expected cross-sections. Figure (b) shows all background process histograms stacked, with the three signal histograms (again scaled according to expected cross-section) superimposed. A vertical line shows the applied event selection, an arrow indicates the part of the distribution that is kept.

5.1.1 Expected Event Yields

The final and intermediate results of the event selection process can be found in Tables 5.2, 5.3, 5.4 and 5.5. A more graphic summary is included in Figure 5.7. The following paragraphs will discuss the contribution of the different event classes and discuss the effectiveness of the different cuts.

For the signal process corresponding to a charged Higgs mass of $m_{H^+}=200$ GeV about 6% of the events are left, the signal acceptance rates increasing for the signals corresponding to higher mass assumptions to up to 11% for $m_{H^+}=600$ GeV. Less than 0.3% of the initial events from the individual background processes remain after the event selection. These remaining events are mainly contributed by the single-top background, yielding about 90% of the total background events. The second strongest remaining background is caused by top quark pair production with a contribution to the total background of about 7%. The remaining background events are contributed by the other event classes. In Table 5.2, it is clearly visible that especially the di-boson and W+jet event categories can be suppressed very effectively. An overview of the absolute values of the remaining events can be found in Table 5.5, showing the expected event yields after each cut.

The cut providing the largest background reduction is the cut in the transverse momentum of the leading tau candidate. As can be seen in Table 5.3, it provides an efficiency of about one third for all signal processes while accepting less than five percent of events from most background categories. The second most effective cut is the one performed in E_T^{miss} as can be seen very well in Figure 5.7. This cut provides a good background reduction as well as a high acceptance rate for the signal processes, which is dependent on the signal mass hypothesis. This dependency shows, that the core area of the signal distributions in E_T^{miss} vary for different mass hypotheses. This makes the missing transverse energy a good candidate for the attempted optimization of event selection parameters as described in Chapter 6. The cut with the least impact on the expected event yields is the cut in $E_T^{\text{sign.}}$. This is to be expected as according to [12] it is intended to suppress multi-jet background not considered in this study.

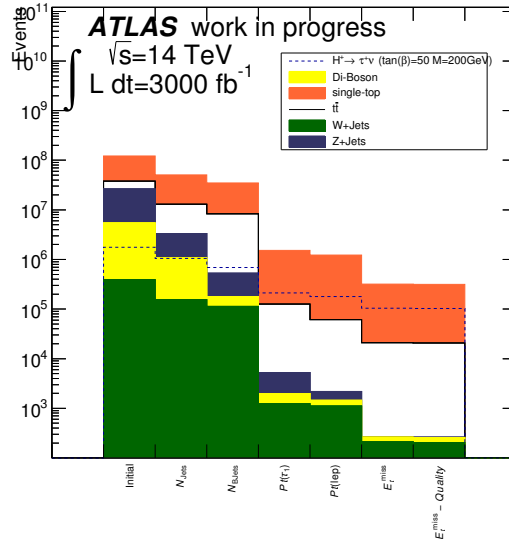


Figure 5.7: Expected event yields for 3000 fb⁻¹ analysis with stacked event numbers for each cut. A single signal histogram for $m_{H^+}=200$ GeV is superimposed for comparison.

Bin	Cut	$H_{200\text{GeV}}^+$	$H_{400\text{GeV}}^+$	$H_{600\text{GeV}}^+$	Di-Boson	Single-t	$t\bar{t}$	Z+Jets	W+Jets
0	<i>Initial</i>	1	1	1	1	1	1	1	1
1	N_{Jets}	0.6	0.63	0.66	0.2	0.57	0.85	0.52	0.054
2	N_{BJets}	0.39	0.42	0.43	0.011	0.38	0.69	0.38	0.0019
3	$Pt(\tau_1)$	0.12	0.14	0.15	0.00012	0.019	0.011	0.0044	1.6e-05
4	N_{lep}	0.1	0.11	0.12	5.3e-05	0.016	0.0052	0.0039	6.1e-06
5	E_t^{miss}	0.059	0.094	0.11	9e-06	0.0042	0.0018	0.00086	2.1e-07
6	$E_T^{\text{miss,sig}}$	0.059	0.093	0.11	9e-06	0.0041	0.0018	0.00083	2.1e-07

Table 5.2: Total efficiencies of event selections for three representative signal hypotheses and considered background processes. The values are calculated as the ratio between the event yield after the cut labeling the line to the initial number of events for the corresponding process.

Bin	Cut	$H_{200\text{GeV}}^+$	$H_{400\text{GeV}}^+$	$H_{600\text{GeV}}^+$	Di-Boson	Single-t	$t\bar{t}$	Z+Jets	W+Jets
1	N_{Jets}	0.6	0.63	0.66	0.2	0.57	0.85	0.52	0.054
2	N_{BJets}	0.65	0.66	0.66	0.054	0.67	0.8	0.72	0.036
3	$Pt(\tau_1)$	0.31	0.34	0.34	0.011	0.051	0.016	0.012	0.0085
4	N_{lep}	0.84	0.82	0.81	0.44	0.82	0.49	0.88	0.38
5	E_t^{miss}	0.58	0.82	0.91	0.17	0.26	0.35	0.22	0.035
6	$E_T^{\text{miss,sig}}$	0.99	0.99	0.99	1	0.99	0.99	0.97	1

Table 5.3: Relative cut efficiencies of event selection process for three representative signal hypotheses and considered background processes. The values are calculated by comparing event yield after the corresponding cut to the prior yield.

Bin	Cut	$H^+_{200\text{GeV}}$	$H^+_{400\text{GeV}}$	$H^+_{600\text{GeV}}$	Complete Background
0	<i>Initial</i>	1751085 ± 2581	74836 ± 107	11099 ± 16	22449800924 ± 27862396
1	N_{Jets}	1055862 ± 2002	47265 ± 85	7289 ± 13	2769799311 ± 2048140
2	N_{BJets}	691297 ± 1620	31104 ± 69	4810 ± 10	1336309915 ± 523117
3	$Pt(\tau_1)$	212893 ± 899	10435 ± 40	1636 ± 6	27152264 ± 58590
4	N_{lep}	178905 ± 824	8589 ± 36	1321 ± 5	16469309 ± 41392
5	E_t^{miss}	103741 ± 628	7068 ± 33	1201 ± 5	5044870 ± 23636
6	$E_T^{\text{miss,sig}}$	102456 ± 624	6990 ± 32	1188 ± 5	4972823 ± 23459

Table 5.4: Overview of the expected event yields and their statistical uncertainties for 3000 fb⁻¹ of all signal hypotheses.

Bin	Cut	$H^+_{200\text{GeV}}$	$H^+_{300\text{GeV}}$	$H^+_{400\text{GeV}}$	$H^+_{500\text{GeV}}$	$H^+_{600\text{GeV}}$	Di-Boson	single-top	$t\bar{t}$
0	<i>Initial</i>	1751085± 2582	246851± 356	74836± 108	26251± 38	11100± 16	62790616± 32282	500767360± 66844	1595560960± 543659
1	N_{Jets}	1055862± 2002	152294± 279	47265± 86	16993± 30	7289± 13	12561871± 14539	285241664± 54582	1361806976± 503384
2	N_{BJets}	691298± 1620	100018± 226	31105± 70	11224± 25	4811± 11	681282± 2932	190817104± 44242	1093209216± 450651
3	$Pt(\tau_1)$	212894± 899	32506± 129	10435± 40	3789± 14	1636± 6	7556± 303	9693916± 9813	16972308± 56522
4	N_{lep}	178906± 824	27055± 117	8590± 37	3093± 13	1322± 6	3306± 194	7951210± 8857	8259447± 39441
5	E_t^{miss}	103741± 628	19878± 101	7068± 33	2704± 12	1201± 5	562± 84	2092647± 4559	2918188± 23027
6	$E_T^{\text{miss,sig}}$	102456± 624	19636± 100	6990± 33	2675± 12	1188± 5	562± 84	2063091± 4527	2876624± 22855

Table 5.5: Overview of the expected event yields and their statistical uncertainties for 3000 fb⁻¹ of all background classes.

5.2 Expected Significance

The distribution of the transverse mass after event selection is used as the final discriminant for the evaluation of the expected sensitivity. The transverse mass is calculated from the visible tau lepton decay p_T and E_T^{miss} , as

$$m_T = \sqrt{2p_T^\tau E_T^{\text{miss}} \cdot (1 - \cos \Delta\phi_{\tau, \text{miss}})}, \quad (5.3)$$

where $\Delta\phi_{\tau, \text{miss}}$ is the azimuthal angle between the hadronically decaying tau lepton and the missing transverse energy vector. This variable corresponds to the projection of the invariant mass of the $(\tau \nu_\tau)$ -system ancestor on the transverse plane. For signal events, this ancestor is the H^+ , while for background events producing a W^\pm boson decaying to $\tau \nu_\tau$ the determined m_T value originates from the W^\pm boson. Figure 5.8 shows the final distribution for this variable after the complete event selection process.

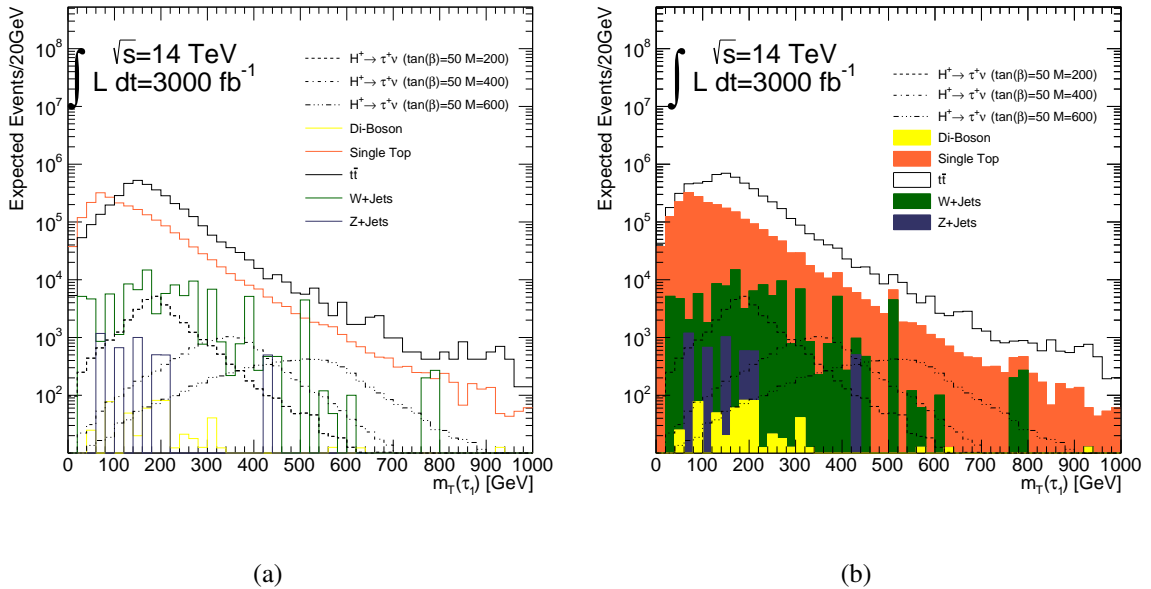


Figure 5.8: Distribution of m_T after the full event selection process. Figure (a) superimposes all background histograms as well as three signal histograms for different m_{H^+} values. All histograms are scaled corresponding to their expected cross-sections.

Figure (b) shows all background process histograms stacked, with the three signal histograms (again scaled according to expected cross-section) superimposed.

A dedicated algorithm based on the asymptotic formulas described in [26] as well as the CLs technique described in [27] is used for further analysis. This asymptotics algorithm uses the yield and shape of provided histograms to calculate limits on the factor of the cross section for H^+ production times the Branching ratio of the decay ($H^+ + \tau \nu_\tau$). This is done under the assumption that only the background processes are realized in nature. The error bands for the returned values are calculated using a set of systematic uncertainties that need to be predefined during the configuration of the algorithm.

Apart from these limits on the production cross section, an estimation of the accessible parameter space regions of the $m_{H^+}^{\text{max}}$ scenario as a physics model prospect is also of interest. As mentioned

earlier, the $m_{H^+}^{\max}$ scenario is a parameter subset of the MSSM which can be described by the two parameters m_{H^+} and $\tan\beta$. For the $m_{H^+}^{\max}$ scenario, theoretical values for $\sigma_{H^+} \times \text{BR}(H^+ \rightarrow \tau + \nu_\tau)$ can be calculated for any combination of m_{H^+} and $\tan\beta$. This knowledge is combined with the experimentally determined limits to allow the determination of regions in the $\tan\beta/m_{H^+}^{\max}$ plane that can be excluded at 95% confidence level.

The results for both of the evaluations described above are acquired using the same tools used in [12]. Corresponding visualized results can be found in Figure 5.9 while the results of [12] concerning heavy charged Higgs bosons are included for comparison in Figure 5.10. A detailed discussion and comparison of all results can be found in Section 5.4.

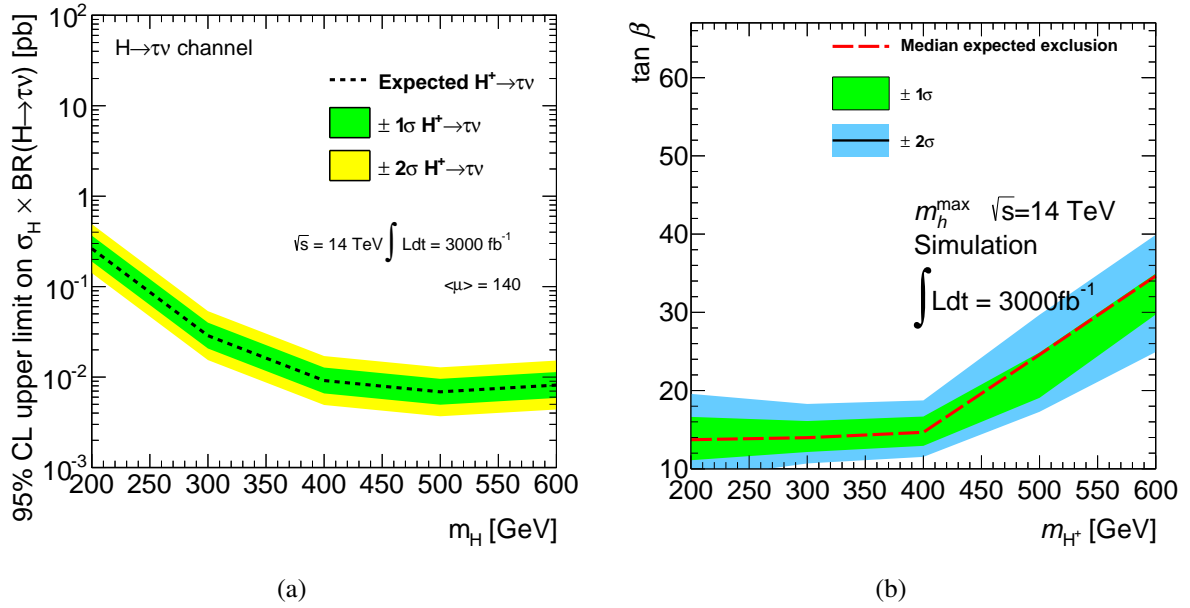


Figure 5.9: Results obtained from applying the analysis process to simulated data for 14 TeV and an integrated luminosity of 3000 fb^{-1} . Figure (a) shows the expected limits on $\sigma_{H^+} \times \text{BR}(H^+ \rightarrow \tau + \nu_\tau)$. Figure (b) shows the expected exclusion ranges in the $\tan\beta/m_{H^+}$ plane of the MSSM. Regions above the dashed line can be excluded at 95% confidence.

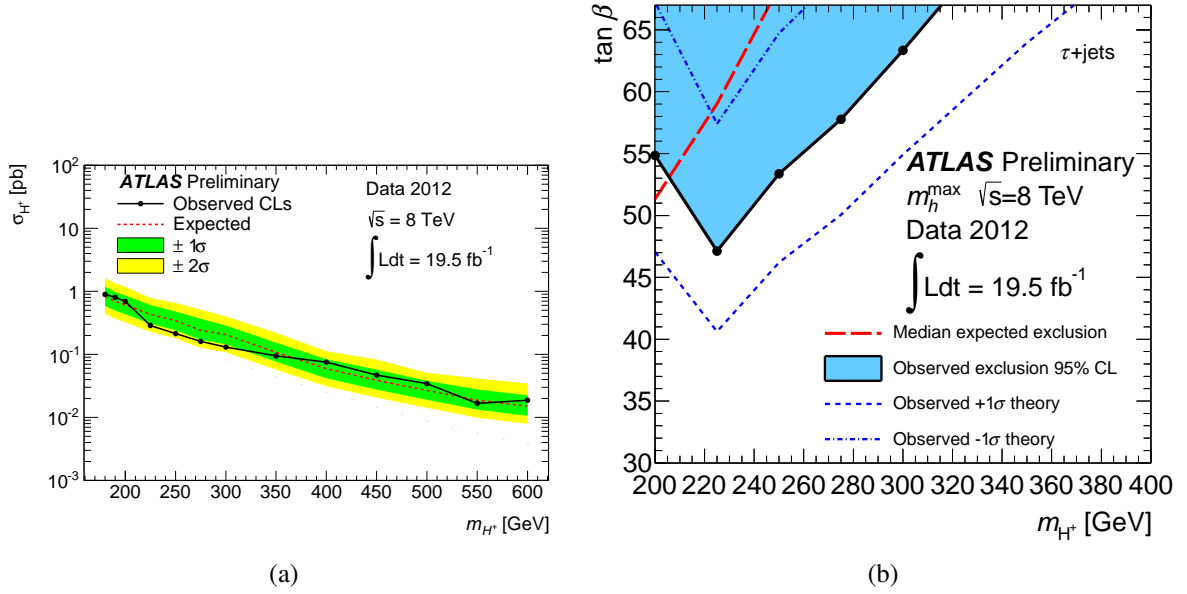


Figure 5.10: Results obtained in [12] on data for 8 TeV and an integrated Luminosity of 19.5 fb^{-1} . Figure (a) shows the expected limits on $\sigma_{H^+} \times \text{BR}(H^+ \rightarrow \tau + \nu_\tau)$. Figure (b) shows the expected exclusion ranges in the $\tan \beta/m_{H^+}$ plane of the MSSM. Regions above the dashed line can be excluded at 95% confidence.

5.3 Search at lower Luminosities

This part of the analysis is designed to evaluate the potential sensitivity increase for Run 3 with 300 fb^{-1} and the lower mean number of interactions $\langle \mu \rangle = 60$ (compared to $\langle \mu \rangle = 140$ for Run 4). To simulate these different conditions, the used histograms are scaled according to the lower number of expected events. Also the different conditions are used to adjust the utilized smearing and reconstruction tools, mainly affecting the determination of the missing transverse energy and the reconstruction of jets, as both of these variables are strongly pileup dependent. The rest of the analysis remains identical to the description provided in the previous parts of this chapter. The resulting limits and $m_{H^+}^{\text{max}}$ exclusion ranges can be found in Figure 5.11.

5.4 Comparison of Sensitivities

This section provides a discussion of the expected improvement in sensitivity for future measurements. Table 5.6 contains the expected limits on $\sigma_{H^+} \times \text{BR}(H^+ \rightarrow \tau + \nu_\tau)$ for the analysis performed in [12] with 19.5 fb^{-1} of data taken at a center of mass energy of $\sqrt{s} = 8 \text{ TeV}$ as well as the results for the expected limits for Runs 3 and 4 at $\sqrt{s} = 14 \text{ TeV}$ with integrated luminosities of 300 fb^{-1} and 3000 fb^{-1} , respectively.

In theory, the sensitivity should be roughly proportional to the significance for a simple counting experiment calculated as $\frac{s}{\sqrt{b}}$ with s and b as the number of signal and background events. This means that for an increase of luminosity by an arbitrary factor x , this significance increases by a factor of \sqrt{x} . A comparison between the baseline results and those expected for LHC Run 3 shows that this is not the case. The limits improve by significantly less than the expected factor $\sqrt{\frac{300}{19.5}} \approx 4$. For the luminosity

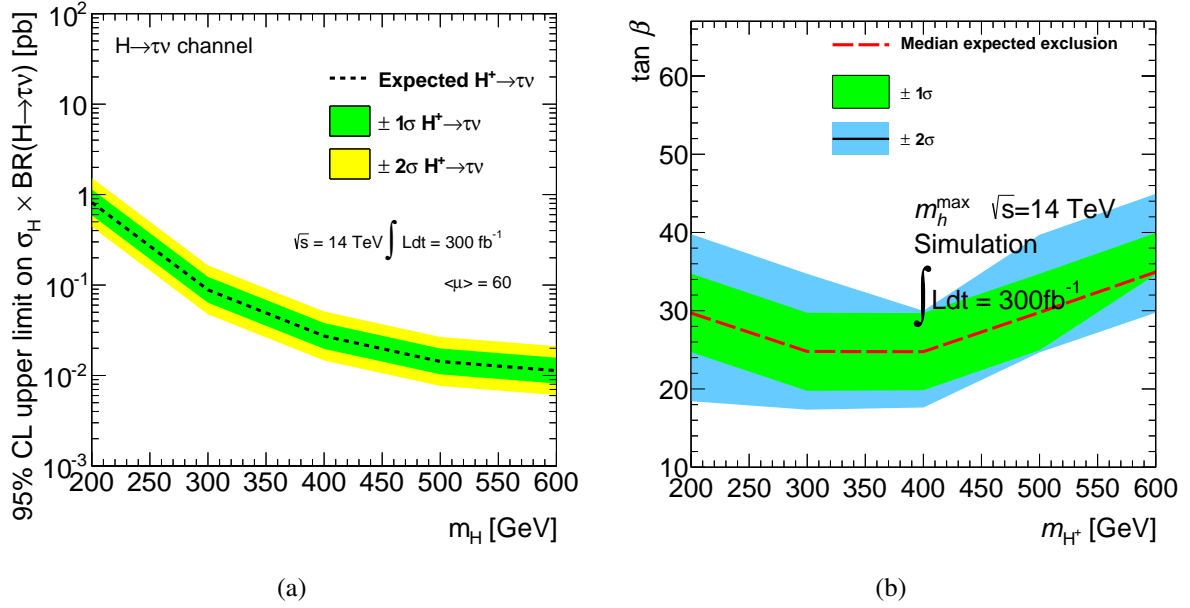


Figure 5.11: Results for sensitivity study for Run 3 with an integrated luminosity of 300 fb^{-1} and $\langle\mu\rangle=60$. Figure (a) shows the expected limits on $\sigma_{H^+} \times \text{BR}(H^+ \rightarrow \tau + \nu_\tau)$. Figure (b) shows the expected exclusion ranges in the $\tan\beta/m_{H^+}$ plane of the MSSM. Regions above the dashed line can be excluded at 95% confidence.

Analysis	$\sigma_{\text{max}}^{200}$ [pb]	$\sigma_{\text{max}}^{300}$ [pb]	$\sigma_{\text{max}}^{400}$ [pb]	$\sigma_{\text{max}}^{500}$ [pb]	$\sigma_{\text{max}}^{600}$ [pb]
Baseline	0.69	0.13	0.075	0.034	0.019
3000fb^{-1}	0.263291	0.028724	0.009158	0.006869	0.008162
300fb^{-1}	0.820161	0.088500	0.027318	0.014289	0.011305

Table 5.6: Expected limits on $\sigma_{H^+} \times \text{BR}(H^+ \rightarrow \tau + \nu_\tau)$

improvement from 300 fb^{-1} to 3000 fb^{-1} would be somewhere around $\sqrt{\frac{3000}{300}} = \sqrt{10} \approx 3$ which is consistent with the improvements observed when comparing the results in the mass ranges from $m_{H^+} = 200 \text{ GeV}$ to $m_{H^+} = 400 \text{ GeV}$. The fact that within our analysis the increased luminosity leads to the expected improvements is an indicator for an additional effect that reduces the expected sensitivity for both Runs 3 and 4 compared to the results from [12]. It is assumed that the responsible difference in the performed analysis are the cross section uncertainties for the background processes required in a simulated analysis. These uncertainties are significantly smaller for the baseline analysis as it is able to precisely estimate background from data. Another effect that can be seen when comparing the limit results for 3000 fb^{-1} and 300 fb^{-1} is that there is almost no improvement for the mass range above $m_{H^+} = 500 \text{ GeV}$. This effect can be seen in both the limits on $\sigma_{H^+} \times \text{BR}(H^+ \rightarrow \tau + \nu_\tau)$ and in the exclusion in the $\tan\beta/m_{H^+}$ plane, it is caused by the fact that increases in luminosity lead to an increase in the expected events dependent on the cross section. The fact that the cross sections for processes corresponding to higher m_{H^+} hypotheses are significantly smaller (two orders of magnitude) than those for processes involving light charged Higgs bosons leads to a greatly reduced improvement in these mass ranges. Nevertheless, this study shows that significant improvements in sensitivity are to be expected for the future runs and especially Run 4. It will be possible to cover large ranges of the MSSM parameter space and hopefully new discoveries will be made.

5.5 Study of different Systematic Uncertainties

When treating uncertainties for the calculation of the final expected limits, the asymptotics tool can distinguish between normalization and shape uncertainties. Overall systematics are assumed to influence the total yield of certain histograms, resulting in a different scaling. Shape uncertainties are modeled more precisely by considering additional histograms with corresponding variations. The original analysis from [12] considers a wide spectrum of uncertainties, both absolute and modeled from histograms. In order to identify the most important uncertainty factors, a study is conducted using configuration files and data from [12]. The expected limits for the different mass points are calculated multiple times, each time omitting a different uncertainty. These modified results are then compared to the limit obtained when all uncertainties are considered. The most important systematic uncertainty categories determined with this method are listed in the following.

- uncertainties affecting energy measurements (BaselineJes, tes, Flavour, BJes, PileupRho, JER)
- identification performance uncertainties for tau leptons and b-jets (tau_id, BJet)
- modeling uncertainties (GenShowering, ISR)

To gain an indicator of how strongly these main uncertainties affect the overall results for different mass points, the variation in the expected limits caused by omitting these uncertainties completely was calculated for the complete mass range for each systematic uncertainty. The results of this can be found in Figure 5.12.

It can be seen that the ISR (Initial State Radiation) systematic provides a deviation of slightly less than five percent for the mass point $m_{H^+}=300$ TeV. Also the "BJet" variation contributes about one percent deviation for each point. Except for these two parameters, all others remain below one percent of contribution. The yield uncertainty for most of these uncertainty categories can be adapted and is used for our calculations. The shape uncertainties can not be considered as the histograms required can not be generated. To evaluate how much this effects our results, the procedure of omitting one contributing shape uncertainty and recalculating the limits is repeated, retaining all yield uncertainties. The results of this procedure are visualized in Figure 5.13. It can be seen that these shape uncertainties do not provide effects as strong as those received from neglecting the total uncertainty. It can be seen that the uncertainty of the "Flavour" systematic is caused mainly by shape properties, while the effect of the initial state radiation uncertainty (ISR) is mostly due to the overall yield.

Of the uncertainties listed above, all except for the Initial State Radiation, and the GenShowering uncertainties are accounted for as yield uncertainties adapted from [12]. It is assumed, that the final results are only affected by the missing ISR and GenShowering uncertainties as well as the missing shape uncertainties. By quadratic addition of the relative uncertainties a combined uncertainty of less than 5% for every mass point is calculated. Our Study additionally uses cross section uncertainties for signal and background processes as the background estimation process used is susceptible to changes in cross section. Also both yield and shape uncertainties for E_T^{miss} are modeled and accounted for.

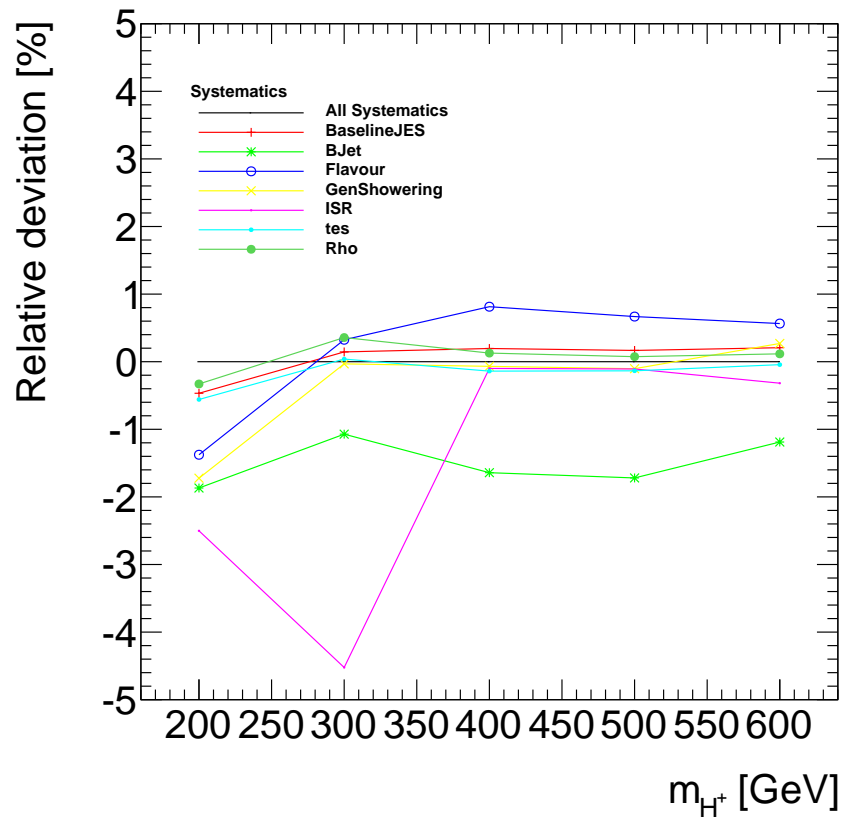


Figure 5.12: Relative deviation caused by different uncertainties in dependence of m_{H^+} . The Standard configuration is shown in the Black line marked "Standard".

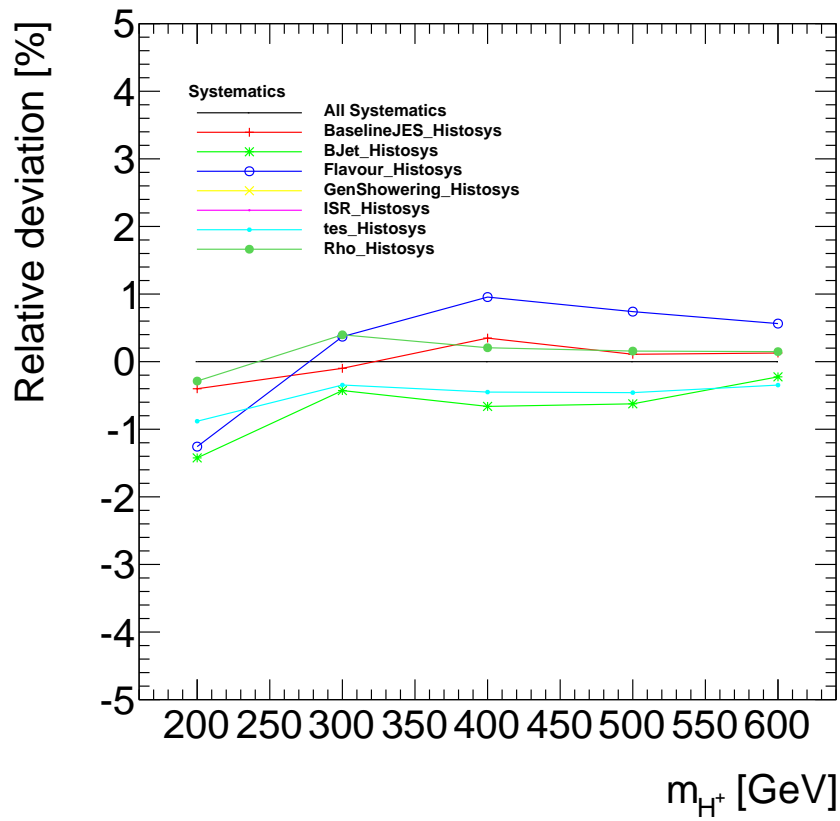


Figure 5.13: Histogram systematics used in [12].

Optimization of Analysis

In this chapter an attempt at optimizing the previously described analysis is made in the hope of improving the limits and exclusion ranges presented in the previous chapter. The goal is to provide an optimized analysis for each mass hypothesis respectively providing a higher sensitivity towards the corresponding signal. The following optimization is based on the assumption that a better ratio between the number of signal and background events should improve the expected sensitivity. As can be seen in Figures 5.3 and 5.5, the shape of the expected signal distribution in the variables p_T and E_T^{miss} shows a dependency on the mass of the assumed charged Higgs boson. This behaviour is exploited in the event selection process, where selection parameters for these variables are adapted to better extract specific mass hypothesis signals. The following sections introduce the tools and figures of merit utilized for this optimization and describe the resulting selection criteria. The optimization is then evaluated with respect to the behavior of expected limits on $\sigma_{H^+} \times \text{BR}(H^+ \rightarrow \tau + \nu_\tau)$ for each of the optimized analyses.

6.1 Mass dependent Optimization

To perform a consistent optimization, a tool which is able to calculate and evaluate a figure of merit for a wide range of possible cut criteria is used. The figure of merit used for this optimization is the so called Asimov significance defined in [26] which is a function of the number of expected events for the signal s and background b defined as:

$$Z = \sqrt{2 \cdot ((s + b) \cdot \ln(1 + s/b) - s)} \quad (6.1)$$

The tool used for this selection parameter analysis evaluates this figure of merit for different cut values and provides a histogram containing this variable in bins corresponding to proposed cut values. This distribution is evaluated, and the cut value corresponding to the maximum of the significance distribution is adopted for the optimized analysis. Table 6.1 shows the values obtained by applying this method to the p_T and E_T^{miss} cuts described in Chapter 5. The results presented include only lower limits for the analyzed criteria. While the possibility of placing upper limits on these variables was also considered and evaluated with the same methods, viable criteria were not found. The figure of merit distributions produced by the tool as well as the shapes of corresponding signal and background distributions can be found in figures 6.2 to 6.6.

m_{H^+} [GeV]	minimum p_T^τ	minimum E_T^{miss}
Standard	40	80
200	90	80
300	130	120
400	170	160
500	200	200
600	250	240

Table 6.1: Cut values after optimizing with significance tools for different signal mass hypotheses. The leftmost column contains the signal towards which the optimization was performed, "Standard" corresponding to the values used in [12]. The other two columns contain the minimum values required in the event selection step of the analysis.

Using the event selection criteria determined with this method, the analysis is repeated for each optimization. A summary of the final event yields for each optimized selection process is included in Table 6.2. As can be seen in this table, the overall significance is increased for every optimized analysis compared to the significance calculated using the corresponding unoptimized signal and background yields. The increase in significance is larger for the higher mass optimizations as is to be expected, as according to [12] the initially used event selection was optimized towards a working point of around $m_{H^+} = 350$ GeV. For the hypotheses of higher boson mass, the optimization yields a much larger increase in significance, almost doubling the final significance for the optimization towards $m_{H^+} = 600$ GeV.

Throughout all improved event selections, the single-top background remains the most dominating background class even though it is reduced significantly for all optimizations. The downside of the increased background reduction can be seen in the signal column, where it is apparent that it comes at the cost of a severe loss in signal yield. For $m_{H^+} = 200$ GeV the optimized event selection removes about 50% more of the signal events. The share of signal reduced by subsequent optimizations is even higher, with only about one thousand signal events passing the selection optimized for $m_{H^+} = 600$ GeV.

With the new final event distributions, the expected sensitivity is determined again as described in Section 5.2. An overview of the values of the limits on $\sigma_{H^+} \times \text{BR}(H^+ \rightarrow \tau + \nu_\tau)$ for the different analyses is given in Table 6.3, the corresponding figures containing the limits on $\sigma_{H^+} \times \text{BR}(H^+ \rightarrow \tau + \nu_\tau)$ at 95% confidence level and the exclusion plots of the $m_{H^+}^{\text{max}}$ scenario are included in Figures 6.7 to 6.7.

Regrettably the optimization does not yield improvements in the expected limits for any optimization apart from that performed to optimize towards the signal corresponding to $m_{H^+} = 200$ GeV (see Figure 6.2). For the other points, the expected cross section limits are larger than those received for the initial analysis for an integrated luminosity of 3000 fb^{-1} as well as the analysis for 300 fb^{-1} . This decline in sensitivity produced by the optimization attempts, shows that improvements in the total significance as defined in Equation 6.1 do not correspond to improvements in the sensitivity of this study. It is assumed that the stricter event selection leads to other effects apart from the increase in significance that result in a loss of sensitivity. As the shape of both signal and background histograms is a vital part in the determination of the final sensitivity, it is assumed that the loss of shape information, inherent to stricter event selection, affects the overall sensitivity far more than the increase in counting significance. For the mass point of $m_{H^+} = 200$ GeV, the improvement gained from the increased significance is assumed to outweigh this loss. The calculated limits on $\sigma_{H^+} \times \text{BR}(H^+ \rightarrow \tau + \nu_\tau)$ for the optimization towards $m_{H^+} = 200$ GeV indicate a higher sensitivity for all signals except that cor-

Opti.	Signal	Background	Di-Boson	Single-top	$t\bar{t}$	W+Jets	Z+Jets	Sig.
CONFNOTE	31091	5914735	587	2091240	3718857	99706	4343	12.77
MH200	15374	1437860	118	814751	588776	33216	997	12.80
CONFNOTE	14201	5914735	587	2091240	3718857	99706	4343	5.84
MH300	3997	438461	52	280646	150669	7093	0	6.03
CONFNOTE	10945	5914735	587	2091240	3718857	99706	4343	4.50
MH400	2280	168331	37	120072	47180	1040	0	5.54
CONFNOTE	8394	5914735	587	2091240	3718857	99706	4343	3.45
MH500	1736	86903	37	64771	21624	470	0	5.87
CONFNOTE	7028	5914735	587	2091240	3718857	99706	4343	2.89
MH600	1134	38908	24	31813	6599	470	0	5.72

Table 6.2: Total number of events remaining after cutting for different mass optimizations. The values in the column labeled "Signal" are the remaining number of events for the signal towards which the optimization was made. Lines labeled "CONFNOTE" contain the values of the analysis of 3000 fb^{-1} with the signal corresponding to the optimization considered in the line below. The rightmost column includes the significance in the final event distributions calculated as defined in Equation 6.1.

Analysis	$\sigma_{\text{max}}^{200}$ [pb]	$\sigma_{\text{max}}^{300}$ [pb]	$\sigma_{\text{max}}^{400}$ [pb]	$\sigma_{\text{max}}^{500}$ [pb]	$\sigma_{\text{max}}^{600}$ [pb]
Baseline	0.69	0.13	0.075	0.034	0.019
3000 fb^{-1}	0.263291	0.028724	0.009158	0.006869	0.008162
300 fb^{-1}	0.820161	0.088500	0.027318	0.014289	0.011305
MH200	0.074733	0.012964	0.014565	0.005554	0.005851
MH300	0.453207	0.132385	0.059612	0.018246	0.012330
MH400	1.095623	0.323711	0.054342	0.017425	0.014098
MH500	3.273263	0.545356	0.080413	0.016111	0.011622
MH600	5.962441	1.168326	0.164942	0.031401	0.011435

Table 6.3: Limits on $\sigma_{H^+} \times \text{BR}(H^+ \rightarrow \tau + \nu_\tau)$ at 95% confidence level for optimized and initial analyses. The label CONFNOTE describes the results obtained in [12]. The results of the 3000 fb^{-1} and 300 fb^{-1} analyses are included for reference, while lines with labels containing mass values are the optimization results of the 3000 fb^{-1} analysis.

responding to the mass point $m_{H^+} = 300 \text{ GeV}$. It is assumed that the increased luminosity assumed by our study provides the capability of using slightly stricter cuts without a loss in sensitivity, as stricter event selection still leaves us with large enough samples to correctly model the shape of occurring distributions. The results of this optimization attempt show that an altered event selection has the potential to increase the overall sensitivity while they also clearly demonstrate that the figure of merit used for optimizing these criteria does not describe the behavior of the expected sensitivity.

The transformation of the limits on $\sigma_{H^+} \times \text{BR}(H^+ \rightarrow \tau + \nu_\tau)$ to the $m_{H^+}^{\text{max}}$ scenarios $m_{H^+}/\tan\beta$ plane reveals a matching behavior for the expected exclusion. Due to the low granularity of this study over the m_{H^+} range, these figures are very susceptible to anomalies in the tools used for visualization. For instance, theoretical values for $\sigma_{H^+} \times \text{BR}(H^+ \rightarrow \tau + \nu_\tau)$ in dependency of $\tan\beta$ and m_{H^+} required for the transformation are only available up to a certain value of $\tan\beta$, causing problems for regions close to boundaries in the theoretical reference values. This can be seen in the behavior of the point for $m_{H^+} = 200 \text{ GeV}$ in Figure 6.5 or the upper mass ranges of Figure 6.2, where the visualization tool

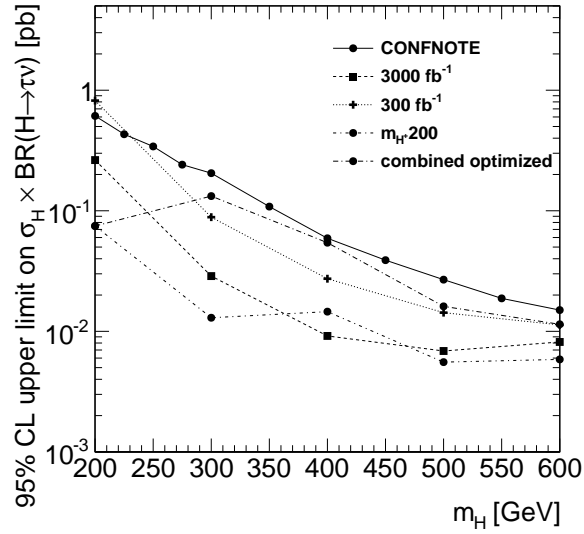


Figure 6.1: Determined limits on $\sigma_{H^+} \times \text{BR}(H^+ \rightarrow \tau + \nu_\tau)$ calculated for different analyses. "CONFNOTE" corresponds to the results of [12]. "3000 fb⁻¹" denotes the main analysis for Run 4 while 300 fb⁻¹ corresponds to the expected limits for Run 3. The graph labeled " $m_{H^+} 200$ " shows the limits obtained from the optimization towards $m_{H^+} = 200$ GeV. The graph titled "combined optimized" is the combination of the limits calculated using the optimization corresponding to the mass point in the graph.

calculates unreasonably small uncertainties even though no comparable behavior can be seen in the matching Figure of the $\sigma_{H^+} \times \text{BR}(H^+ \rightarrow \tau + \nu_\tau)$ limit.

As for the limits on $\sigma_{H^+} \times \text{BR}(H^+ \rightarrow \tau + \nu_\tau)$, the values optimized using the signal hypothesis for $m_{H^+} = 200$ GeV show the highest sensitivity, allowing almost the whole parameter space to be excluded (see Figure 6.7). The subsequent optimizations all result in reduced sensitivities caused by the loss of shape information as discussed above. It can be seen that this degradation is weaker in the regions towards which the optimization was performed. Nevertheless no additional significant improvement is gained from the optimization.

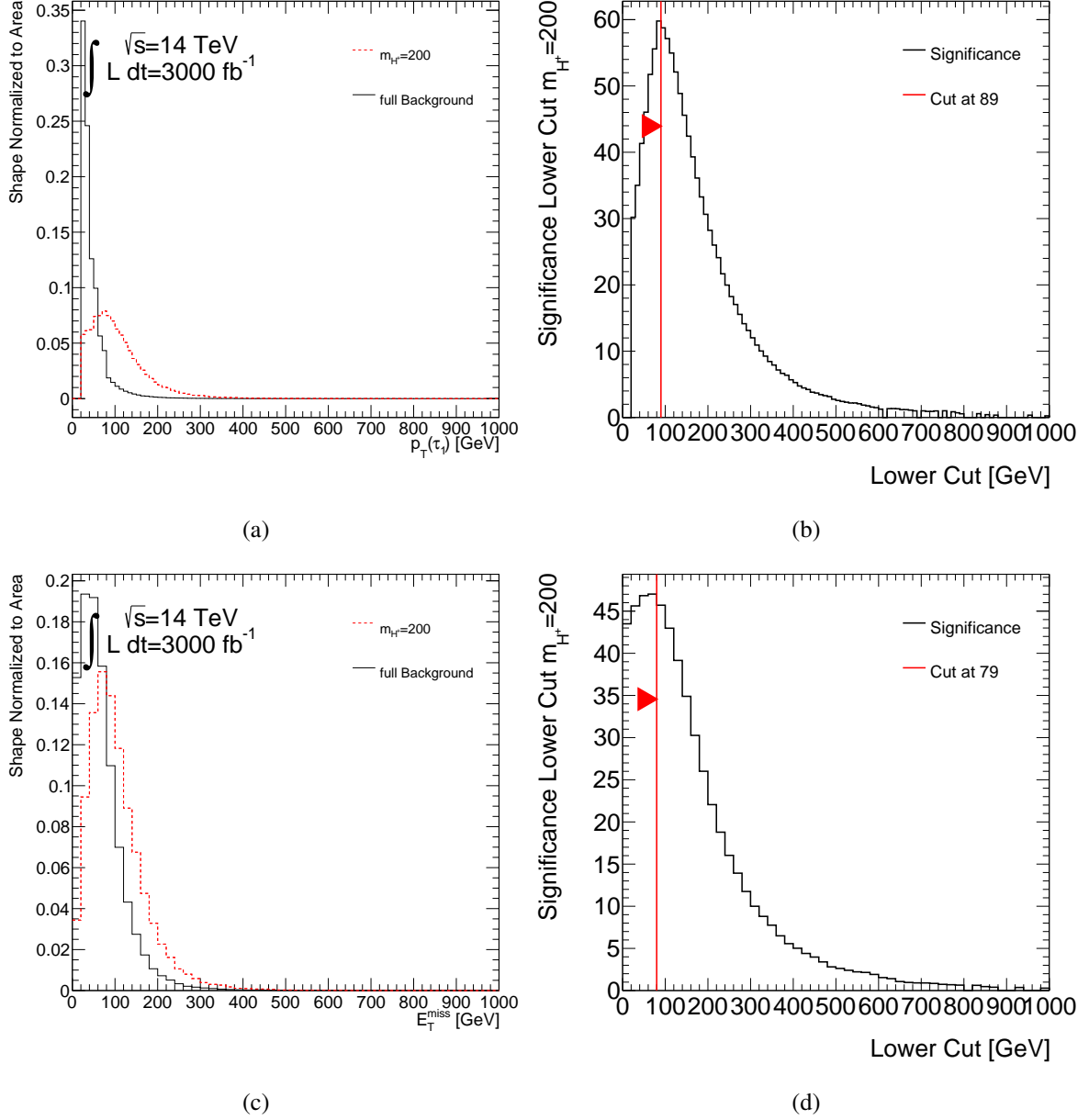


Figure 6.2: Significance Plots for mass hypothesis $m_{H^+} = 200$ TeV. Figures (a) and (b) correspond to the optimization of the p_T^{τ} cut. Figures (c) and (d) show the optimization of the E_T^{miss} criterion as described in 5.1. The left hand figures show a comparison of the shape of background and signal events, the histograms are normalized. The right handed show the significance for different cut values of p_T^{τ} and E_T^{miss} respectively. The assumed optimal value is marked by a vertical line with an arrow indicating the parts of the distribution to keep.

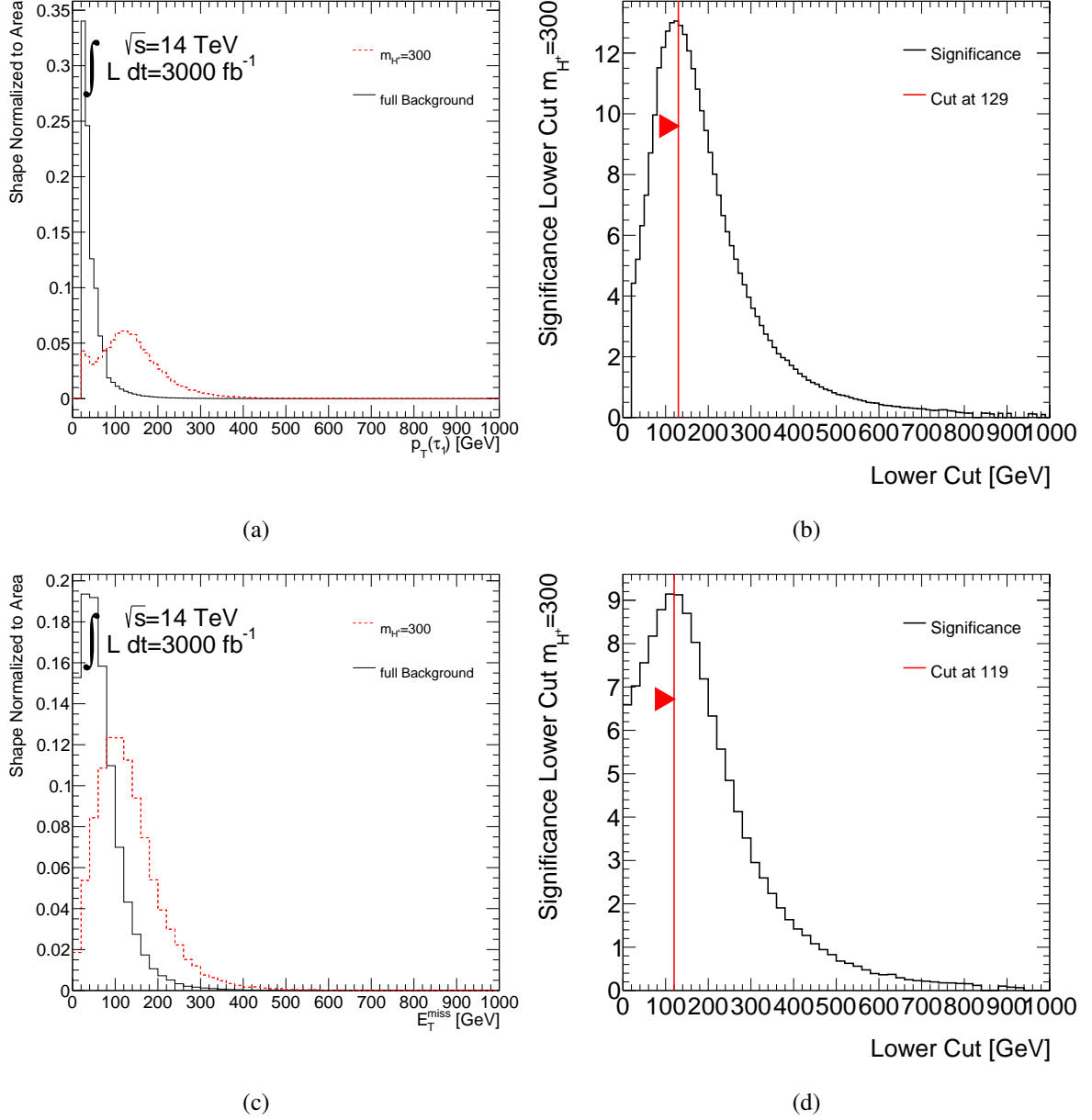


Figure 6.3: Significance Plots for mass hypothesis $m_{H^+} = 300$ TeV. Figures (a) and (b) correspond to the optimization of the p_T^{τ} cut. Figures (c) and (d) show the optimization of the E_T^{miss} criterion as described in 5.1. The left hand figures show a comparison of the shape of background and signal events, the histograms are normalized. The right handed show the significance for different cut values of p_T^{τ} and E_T^{miss} respectively. The assumed optimal value is marked by a vertical line with an arrow indicating the parts of the distribution to keep.

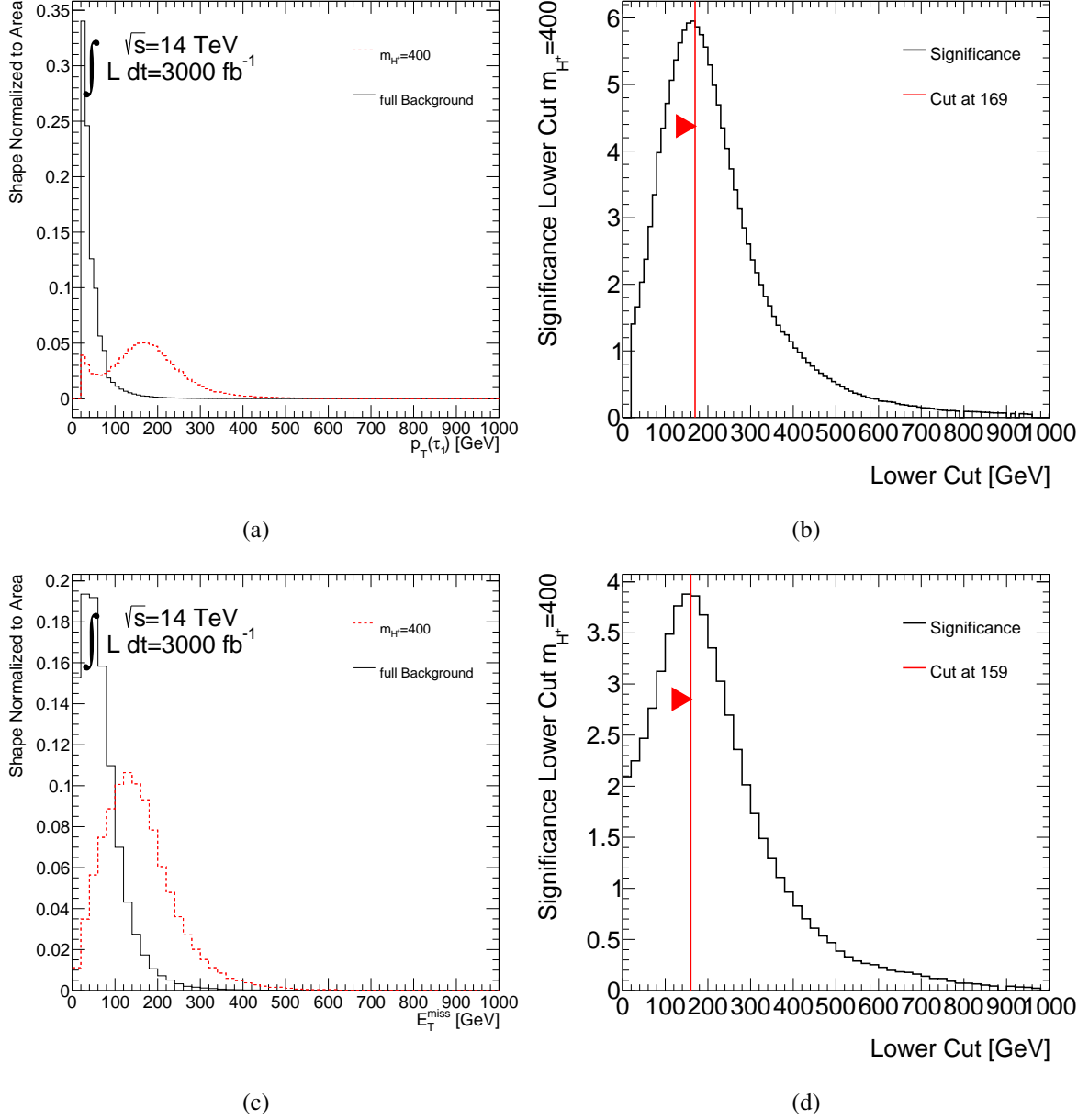


Figure 6.4: Significance Plots for mass hypothesis $m_{H^+} = 400$ TeV. Figures (a) and (b) correspond to the optimization of the p_T^τ cut. Figures (c) and (d) show the optimization of the E_T^{miss} criterion as described in 5.1. The left hand figures show a comparison of the shape of background and signal events, the histograms are normalized. The right handed show the significance for different cut values of p_T^τ and E_T^{miss} respectively. The assumed optimal value is marked by a vertical line with an arrow indicating the parts of the distribution to keep.

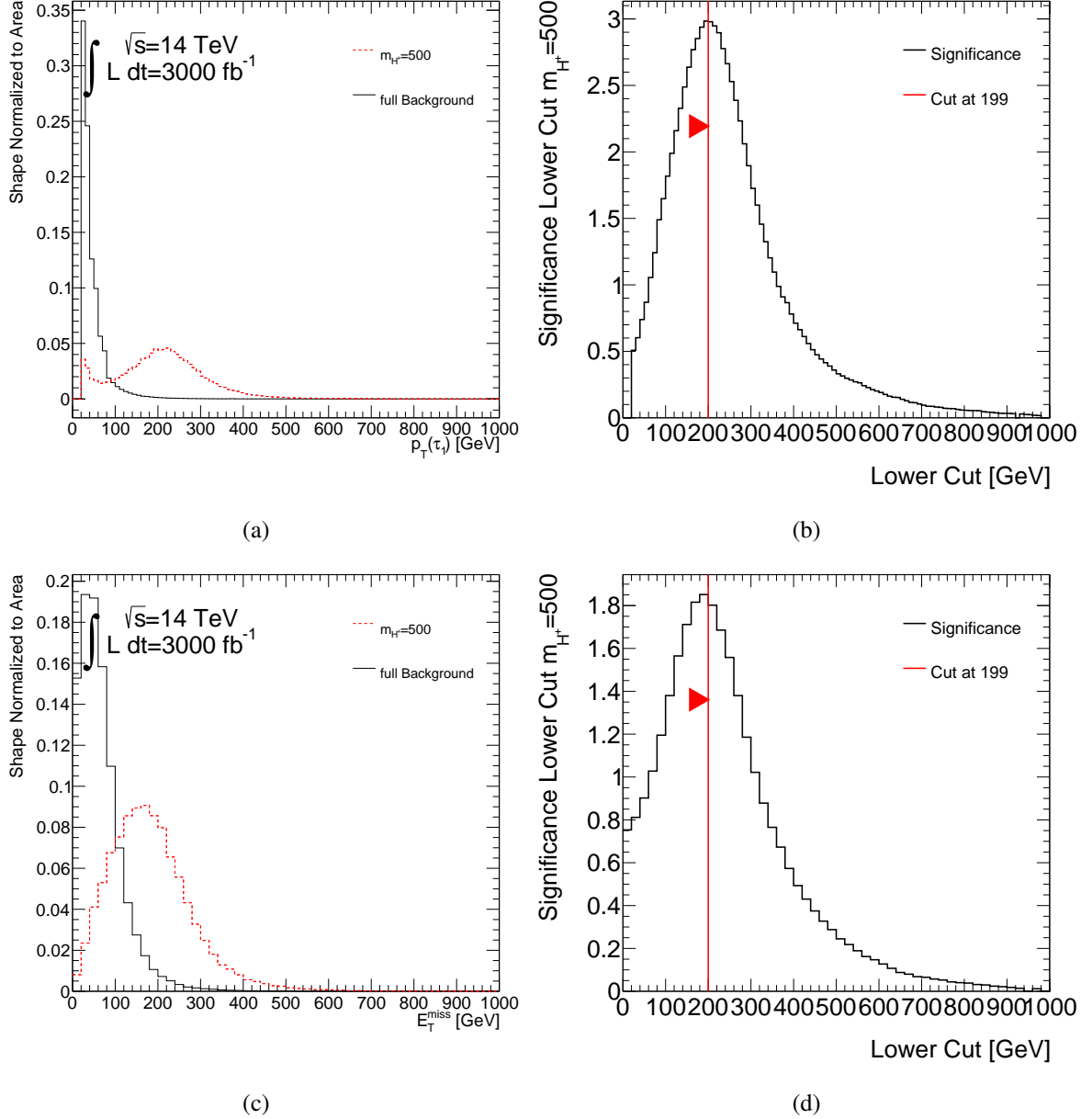


Figure 6.5: Significance Plots for mass hypothesis $m_{H^+} = 500$ TeV. Figures (a) and (b) correspond to the optimization of the p_T^{τ} cut. Figures (c) and (d) show the optimization of the E_T^{miss} criterion as described in 5.1. The left hand figures show a comparison of the shape of background and signal events, the histograms are normalized. The right handed show the significance for different cut values of p_T^{τ} and E_T^{miss} respectively. The assumed optimal value is marked by a vertical line with an arrow indicating the parts of the distribution to keep.

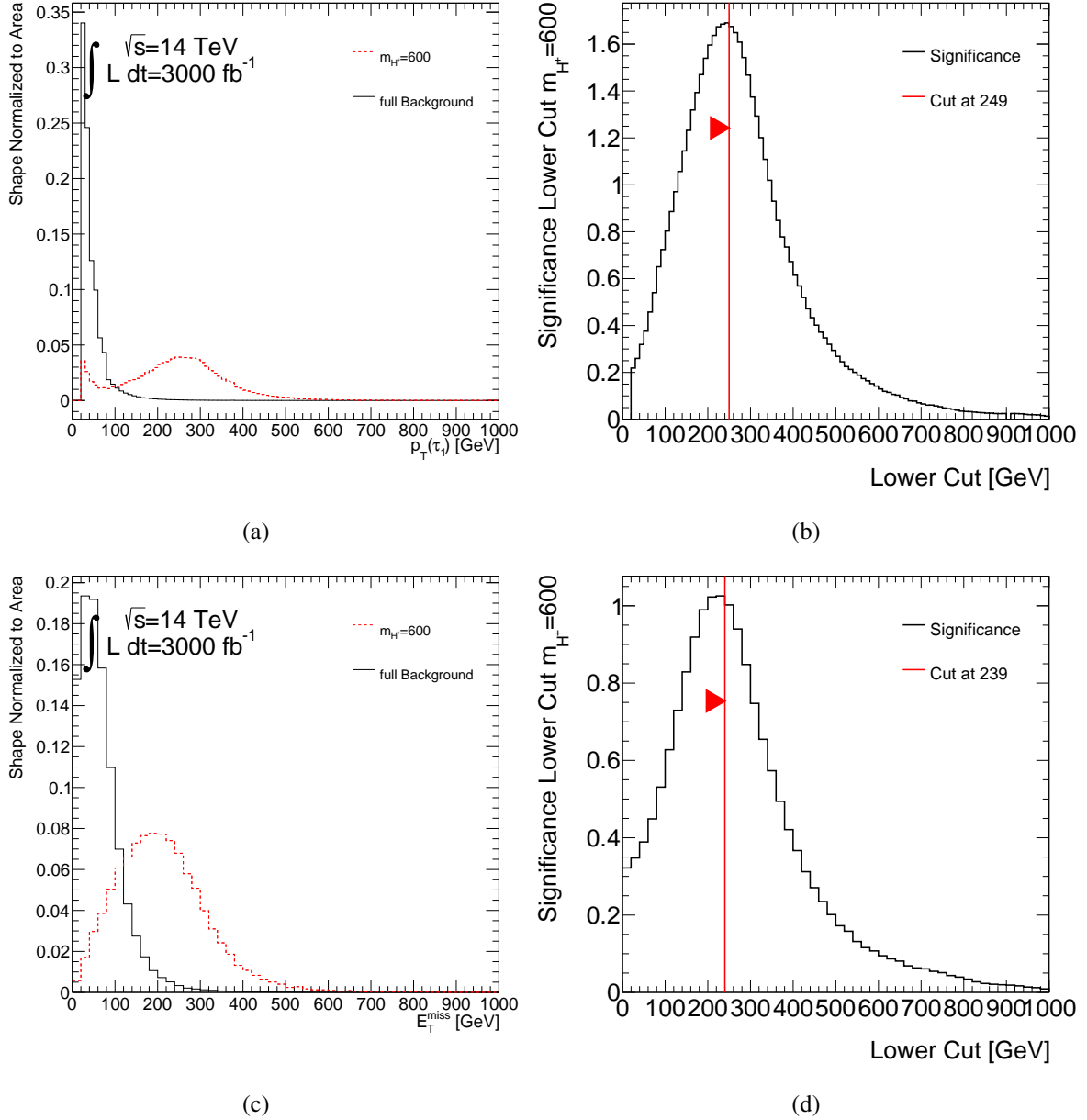


Figure 6.6: Significance Plots for mass hypothesis $m_{H^+} = 600$ TeV. Figures (a) and (b) correspond to the optimization of the p_T^{τ} cut. Figures (c) and (d) show the optimization of the E_T^{miss} criterion as described in 5.1. The left hand figures show a comparison of the shape of background and signal events, the histograms are normalized. The right handed show the significance for different cut values of p_T^{τ} and E_T^{miss} respectively. The assumed optimal value is marked by a vertical line with an arrow indicating the parts of the distribution to keep.

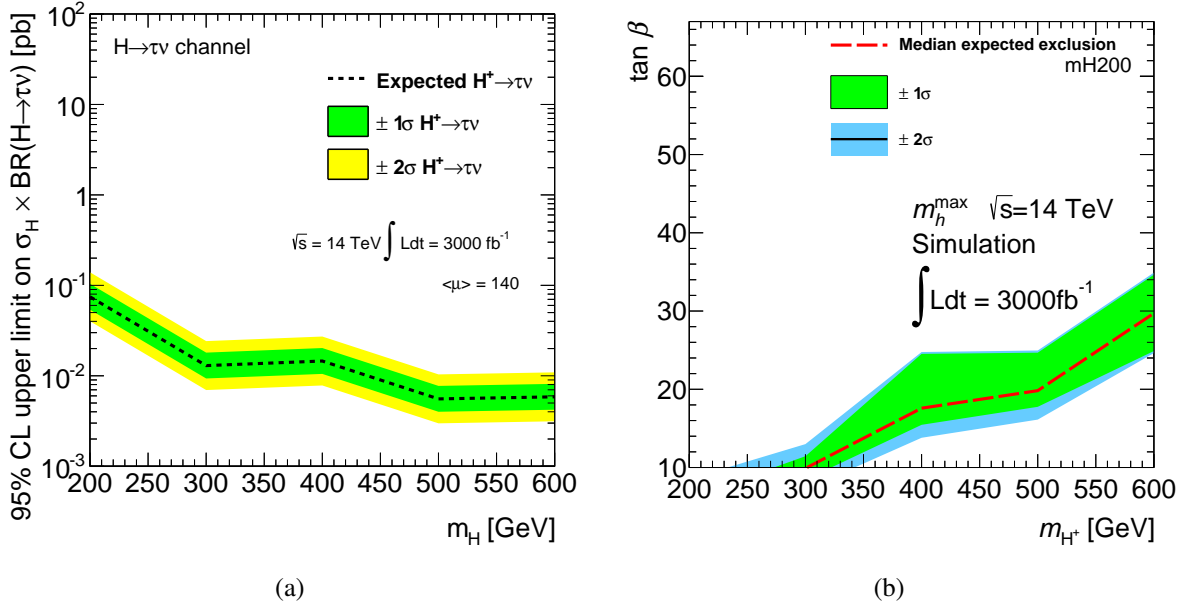


Figure 6.7: Results of the optimization attempt using the hypothesis $m_{H^+} = 200$ GeV. Figure (a) shows the expected limits on $\sigma_{H^+} \times BR(H^+ \rightarrow \tau + \nu_\tau)$. Figure (b) shows the expected exclusion ranges in the $\tan \beta / m_{H^+}$ plane of the MSSM. Regions above the dashed line can be excluded at 95% confidence. The point for $m_{H^+} = 200$ GeV in Figure (b) can be excluded even below $\tan \beta = 10$.

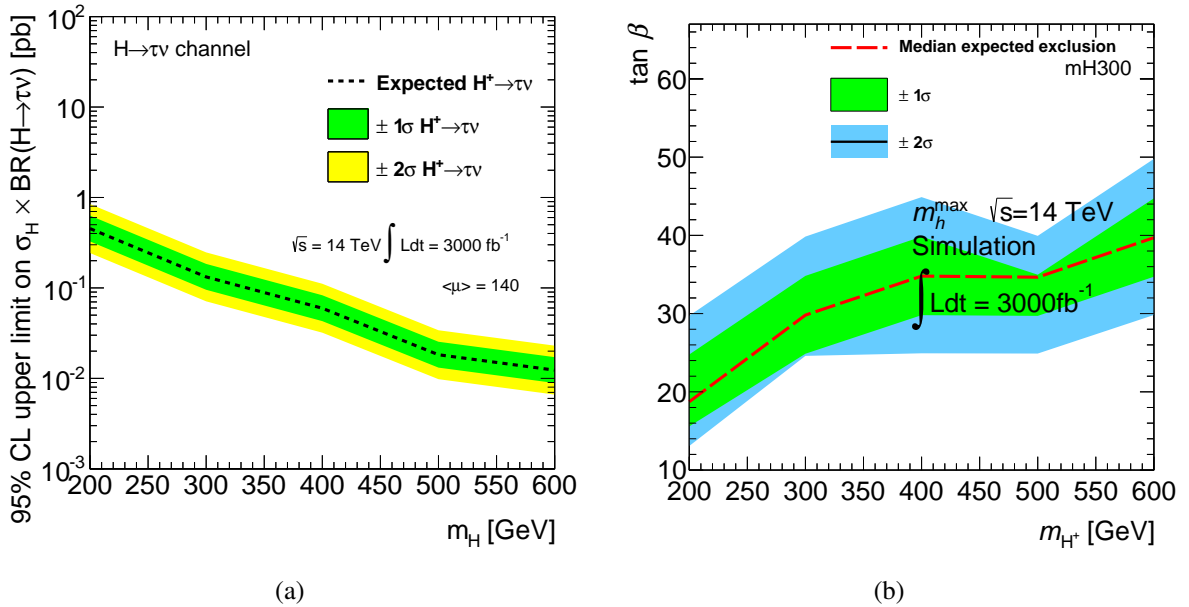


Figure 6.8: Results of the optimization attempt using the hypothesis $m_{H^+} = 300$ GeV. Figure (a) shows the expected limits on $\sigma_{H^+} \times BR(H^+ \rightarrow \tau + \nu_\tau)$. Figure (b) shows the expected exclusion ranges in the $\tan \beta / m_{H^+}$ plane of the MSSM. Regions above the dashed line can be excluded at 95% confidence.

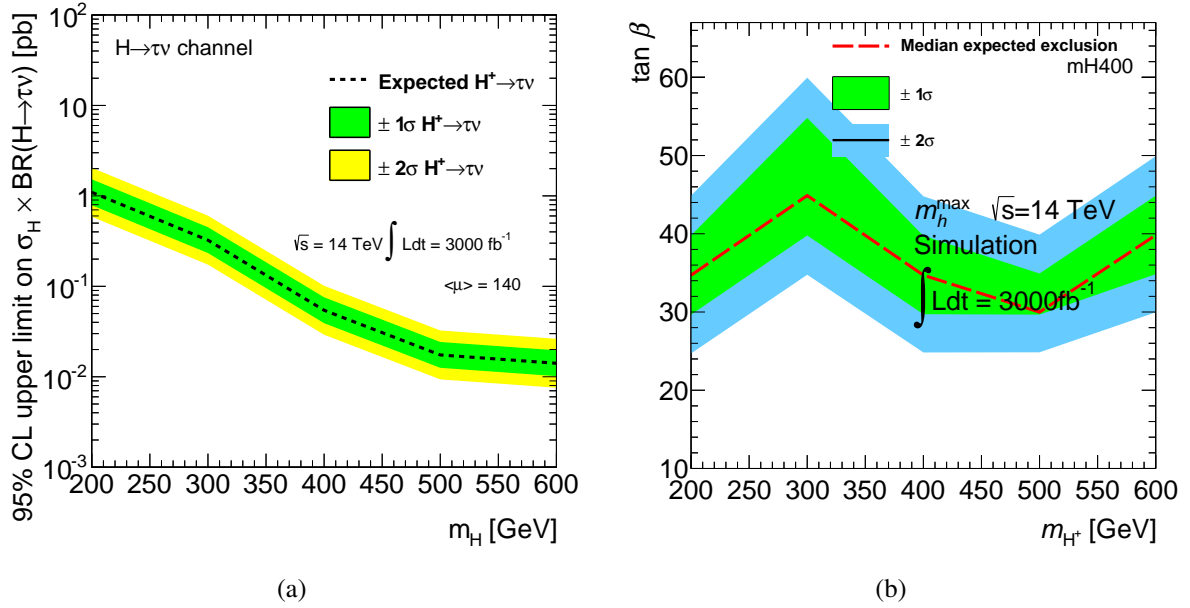


Figure 6.9: Results of the optimization attempt using the hypothesis $m_{H^+} = 400$ GeV. Figure (a) shows the expected limits on $\sigma_{H^+} \times \text{BR}(H^+ \rightarrow \tau + \nu_\tau)$. Figure (b) shows the expected exclusion ranges in the $\tan \beta/m_{H^+}$ plane of the MSSM. Regions above the dashed line can be excluded at 95% confidence.

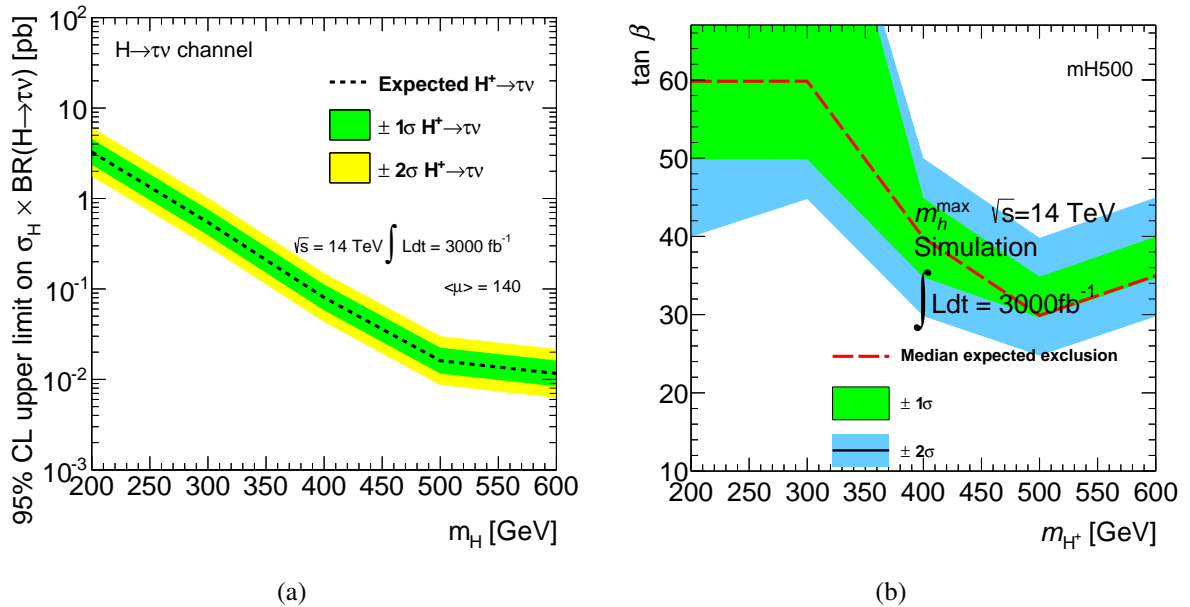


Figure 6.10: Results of the optimization attempt using the hypothesis $m_{H^+} = 500$ GeV. Figure (a) shows the expected limits on $\sigma_{H^+} \times \text{BR}(H^+ \rightarrow \tau + \nu_\tau)$. Figure (b) shows the expected exclusion ranges in the $\tan \beta/m_{H^+}$ plane of the MSSM. Regions above the dashed line can be excluded at 95% confidence.

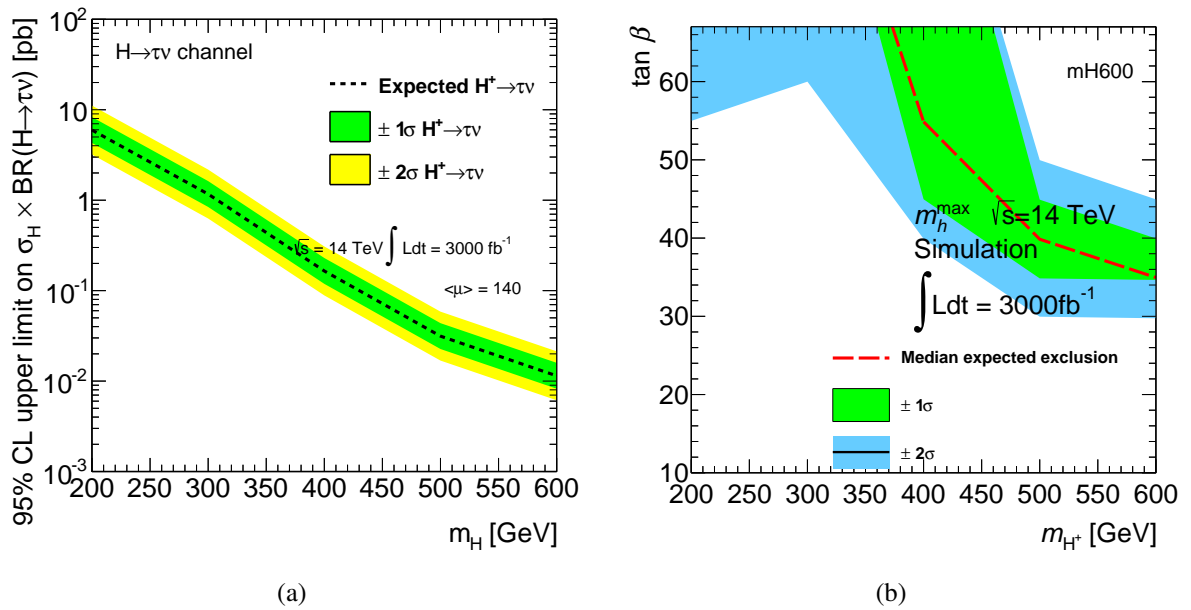


Figure 6.11: Results of the optimization attempt using the hypothesis $m_{H^+} = 600 \text{ GeV}$. Figure (a) shows the expected limits on $\sigma_{H^+} \times \text{BR}(H^+ \rightarrow \tau + \nu_\tau)$. Figure (b) shows the expected exclusion ranges in the $\tan \beta / m_{H^+}$ plane of the MSSM. Regions above the dashed line can be excluded at 95% confidence.

Conclusion

In this study, the sensitivity of the ATLAS experiment towards charged Higgs bosons during Run 3 and Run 4 of the LHC was examined, using Monte Carlo simulated data sets and a fast detector simulation based on parametrisations of measurement resolution and reconstruction efficiency. A mass range from $m_{H^+} = 200$ GeV to 600 GeV was covered. The analysis of this simulated data was performed by adapting methods from a preexisting analysis conducted by members of the ATLAS collaboration. The conducted study consists of the previously mentioned detector simulation, an event selection process designed to reduce the number of background events as well as a statistical evaluation of a final discriminant. With the help of the final discriminant, the expected limits on the factor of the cross section for charged Higgs boson production via $t \rightarrow bH^+$ times the branching ratio for decay via $H^+ \rightarrow \tau\nu_\tau$ can be calculated. The information contained in these limits can be combined with current theoretical findings to provide expected exclusion ranges in the $\tan\beta/m_{H^+}$ plane of the $m_{H^+}^{\max}$ scenario. The examination of the expected limits on $\sigma_{H^+} \times \text{BR}(H^+ \rightarrow \tau + \nu_\tau)$ and the expected excluded parameter regions of the $m_{H^+}^{\max}$ scenario warrants a significant improvement in sensitivity compared to current findings. This improvement is not as large as would be expected considering the increase in luminosity. This is attributed to simulation based uncertainties, that are much smaller for an analysis of detector data. Within the simulation based analysis, the improvement is consistent with the theoretical expectations, yielding an improvement of the sensitivity by about factor three between Runs 3 and 4.

In addition to the directly adapted analysis, an attempt was made to optimize the event selection thresholds for the transverse momentum of the leading tau lepton and the missing transverse energy, in order to enable a dedicated event selection for different hypotheses of m_{H^+} . This optimization did lead to a clearly visible increase in the statistical significance. For one set of optimized selection criteria definite improvements in sensitivity could be observed, while the other sets of optimized parameters led to decreased sensitivity compared to the non optimized values. This behavior is assumed to originate from the fact that the figure of merit used for optimization does not consider the shape information contained in the final distributions for the assessment of the possible criteria. The loss in shape information produced by the optimization process leads to a loss in sensitivity that can not be compensated by improvements from the higher statistical significance.

As some of the systematic uncertainties considered in the initial analysis can not be adopted, an additional study was performed to assess the consequences of this fact. Using the original data from the initial analysis, the relative changes in the expected limits on $\sigma_{H^+} \times \text{BR}(H^+ \rightarrow \tau + \nu_\tau)$ caused

by omitting these uncertainties were assessed. Over the whole mass range from $m_{H^+} = 200$ GeV to 600 GeV, no changes of more than 5% were found.

It is expected, that even in Run 3, a significantly large region of the $m_{H^+}^{\max}$ scenario parameter space will be accessible. In the lower mass ranges, the increase in luminosity provides large improvements, while for the higher masses, higher center of mass energies are needed to provide a significant increase in sensitivity. This behavior is attributed to the fact that an increased luminosity provides cross section dependent increase in the number of expected events. As the cross section of the signal processes containing heavier charged Higgs bosons are very small, significant improvements solely due to higher luminosities do not occur in these mass ranges.

Altogether, a greatly improved sensitivity is expected for the future Runs of the LHC. Whether discoveries indicating supersymmetry or other advanced models will be made is yet to be seen.

Zusammenfassung

In dieser Studie wurde die Sensitivität des ATLAS-Experiments in Bezug auf geladene Higgs-Bosonen während Run 3 und Run 4 des LHC anhand von Monte-Carlo simulierten Daten ermittelt, wobei ein Massenbereich von $m_{H^+} = 200 \text{ GeV}$ bis 600 GeV abgedeckt wurde. Mittels Parametrisierungen der Messauflösung und Rekonstruktionseffizienz wurde das Verhalten des des ATLAS Detektors emuliert.

Zur Untersuchung der simulierten Daten wurden Parameter einer bereits vorhandenen Analyse der ATLAS Kollaboration übernommen. Die durchgeführte Analyse besteht aus der erwähnten Detektor-simulation, einer Ereignisselektion zur Untergrundunterdrückung sowie einer statistischen Auswertung einer finalen Diskriminanten. Mit Hilfe dieser finalen Diskriminanten lassen sich Grenzen auf den Faktor aus dem Wirkungsquerschnitt für die Produktion von geladenen Higgs Bosonen mal dem Verzweigungsverhältnisses des Zerfalls $H^+ \rightarrow \tau\nu_\tau$ errechnen. Die Information aus diesen Grenzen lässt sich mit theoretischen Kenntnissen verknüpfen um ausschließbare Bereiche der $\tan\beta/m_{H^+}$ Ebene des $m_{H^+}^{\max}$ Szenarios zu bestimmen.

Anhand der erwarteten Grenzen für $\sigma_{H^+} \times \text{BR}(H^+ \rightarrow \tau + \nu_\tau)$ und den erwarteten ausschließbaren Parameterregionen de $m_{H^+}^{\max}$ Szenarios lässt sich eine deutliche Sensitivitätsverbesserung gegenüber den aktuellen Ergebnissen erkennen. Die Verbesserung im Vergleich zu den bisherige Ergebnissen fällt hierbei geringer aus als man aus theoretischen Überlegungen anhand der Luminositätssteigerung erwarten würde. Dies wird auf simulationsbedingte systematische Unsicherheiten zurückgeführt die für eine Analyse mit Detektordaten signifikant kleiner sind. Vergleicht man das Sensitivitätsverhalten innerhalb der simulationsbasierten Analyse beobachtet man eine Verbesserung um einen Faktor von ungefähr drei zwischen Run 3 und Run 4, was auch den Erwartungen entspricht.

Zusätzlich zur den übernommen Analyseparametern wurde ein Optimierungsversuch für Ereigniselektionskriterien durchgeführt, mit dem Ziel eine angepasste und damit auch sensitivere Analyse für jeden der untersuchten Massenpunkte zu ermöglichen. Diese Optimierung führte zu einer deutlich erkennbaren Verbesserung der statistischen Signifikanz. Für einen Satz optimierter Parameter ließ sich eine deutliche Verbesserung der Sensitivität erkennen, allerdings zeigten die anderen Optimierungspunkte trotz noch größerer Signifikanzverbesserung einen Sensitivitätsverlust gegenüber den nicht optimierten Kriterien. Dieses Verhalten wird der Tatsache zugeschrieben, dass das zur Optimierung verwendete Gütekriterium, die Asimov-Signifikanz, Forminformationen der finalen Verteilungen nicht in die Bewertung der untersuchten Schnitte mit einbezieht. Der durch die Optimierung verursachte Verlust dieser Forminformationen geht mit einem Sensitivitätsverlust einher der vor allem für die Optimierungen anhand von massereichen Signalhypothesen nicht durch die Verbesserung

aufgrund der erhöhten statistischen Signifikanz ausgeglichen werden kann.

Da einige der in der Ausgangsanalyse berücksichtigten systematischen Unsicherheiten nicht übernommen wurden konnten, wurde eine zusätzliche Studie zur Bestimmung dieser Einflüsse durchgeführt. Anhand der Originaldaten der Ausgangsanalyse wurde die Relative Änderung der erwarteten Grenzen auf $\sigma_{H^+} \times \text{BR}(H^+ \rightarrow \tau + \nu_\tau)$ durch die Vernachlässigung dieser Unsicherheiten bestimmt. Dabei ergab sich im gesamten Massebereich von $m_{H^+} = 200 \text{ GeV}$ bis 600 TeV keine Abweichung von über 5%.

Es wird erwartet, dass bereits während Run 3 ein signifikant größerer Bereich des Parameterraumes des $m_{H^+}^{\text{max}}$ Szenarios zugänglich sein wird als bisher. Im niedrigeren Massenbereich liefert die Erhöhung der Luminosität große Verbesserungen, während im höheren Massenbereich Erhöhungen der Schwerpunktsenergie notwendig sind um einen signifikanten Sensitivitätsgewinn zu erreichen. Dieses Verhalten wird der Tatsache zugeschrieben, dass Luminositäts erhöhungen die erwarteten Ereigniszahlen nur in Abhängigkeit der jeweiligen Wirkungsquerschnitte erhöhen. Da die Wirkungsquerschnitte der Signalprozesse denen Hypothesen von hohen m_{H^+} Werten zugrunde liegen nur sehr klein sind bleibt hier eine signifikante Verbesserung durch reine Luminositätssteigerung aus.

Insgesamt ist jedoch mit einer bedeutend höheren Sensitivität zu rechnen. Ob während der kommenden Jahrzehnte Entdeckungen mit Indizien für Supersymmetrie oder andere erweiterte Modelle gemacht werden bleibt abzuwarten.

Bibliography

- [1] S. Glashow, “Partial Symmetries of Weak Interactions”, *Nucl.Phys.* 22 (1961) pp. 579–588.
- [2] S.L. Glashow, J. Iliopoulos, and L. Maiani, “Weak Interactions with Lepton-Hadron Symmetry”, *Phys. Rev. D* 2 (1970) 1285–1292.
- [3] A. Salam, “Weak and Electromagnetic Interactions”
(), originally printed in Svartholm: Elementary Particle Theory, Proceedings Of The Nobel Symposium Held 1968 At Lerum, Sweden. Stockholm 1968, 367-377.
- [4] S. Weinberg, “A Model of Leptons”, *Phys. Rev. Lett.* 19 (1967) 1264–1266.
- [5] P. W. Higgs, “Broken Symmetries and the Masses of Gauge Bosons”,
Phys. Rev. Lett. 13 (1964) pp. 508–509.
- [6] F. Englert and R. Brout, “Broken Symmetry and the Mass of Gauge Vector Mesons”,
Phys. Rev. Lett. 13 (1964) pp. 321–323.
- [7] G. S. Guralnik, C. R. Hagen, and T. W. B. Kibble, “Global Conservation Laws and Massless Particles”,
Phys. Rev. Lett. 13 (20 1964) pp. 585–587.
- [8] The ATLAS Collaboration, “Observation of a new particle in the search for the Standard Model Higgs boson with the ATLAS detector at the LHC”,
Physics Letters B 716.1 (2012) pp. 1–29.
- [9] The CMS Collaboration, “Observation of a new boson at a mass of 125 GeV with the CMS experiment at the LHC”,
Phys.Lett. B716 (2012) pp. 30–61, arXiv: [1207.7235](https://arxiv.org/abs/1207.7235) [[hep-ex](#)].
- [10] The ATLAS Collaboration, “Performance assumptions based on full simulation for an upgraded ATLAS detector at a High-Luminosity LHC”,
tech. rep. ATL-PHYS-PUB-2013-009, CERN, Sept. 2013.
- [11] The ATLAS Collaboration, “Performance assumptions for an upgraded ATLAS detector at a High-Luminosity LHC”,
tech. rep. ATL-PHYS-PUB-2013-004.
- [12] The ATLAS Collaboration, “Search for charged Higgs bosons in the τ +jets final state with pp collision data recorded at $\sqrt{s} = 8$ TeV with the ATLAS experiment”,
ATLAS-CONF-2013-090.
- [13] J. Beringer et al., “Review of Particle Physics (RPP)”, *Phys.Rev.* D86 (2012) p. 010001.
- [14] A. Djouadi, “The Anatomy of electro-weak symmetry breaking. I: The Higgs boson in the standard model”, *Phys.Rept.* 457 (2008) pp. 1–216, arXiv: [hep-ph/0503172](https://arxiv.org/abs/hep-ph/0503172) [[hep-ph](#)].

- [15] A. Djouadi, “The Anatomy of electro-weak symmetry breaking. II. The Higgs bosons in the minimal supersymmetric model”, *Phys.Rept.* 459 (2008) pp. 1–241, arXiv: [hep-ph/0503173 \[hep-ph\]](#).
- [16] H. v. Radziewski, “Search for Neutral Higgs Bosons of the Minimal Supersymmetric Standard Model in the tau_e tau_mu Decay Mode at sqrt(s) = 7 TeV with the ATLAS Detector”, PhD Thesis: Albert-Ludwigs-Universität Freiburg, 2014, URL: <http://www.freidok.uni-freiburg.de/volltexte/9487/>.
- [17] J. Glatzer, “Search for Neutral MSSM Higgs Bosons Decaying to tau_had tau_had in sqrt(s) = 7 TeV Proton-Proton Collisions with the ATLAS Detector”, PhD Thesis: Albert-Ludwigs-Universität Freiburg, 2013, URL: <http://www.freidok.uni-freiburg.de/volltexte/9204/>.
- [18] The ATLAS Collaboration, “The ATLAS Experiment at the CERN Large Hadron Collider”, *Journal of Instrumentation* 3.08 (2008) S08003, URL: <http://stacks.iop.org/1748-0221/3/i=08/a=S08003>.
- [19] N. Kidonakis, “NNLL resummation for s-channel single top quark production”, *Phys.Rev.* D81 (2010) p. 054028, arXiv: [1001.5034 \[hep-ph\]](#).
- [20] N. Kidonakis, “Next-to-next-to-leading-order collinear and soft gluon corrections for t-channel single top quark production”, *Phys.Rev.* D83 (2011) p. 091503, arXiv: [1103.2792 \[hep-ph\]](#).
- [21] N. Kidonakis, “Two-loop soft anomalous dimensions for single top quark associated production with a W- or H-”, *Phys.Rev.* D82 (2010) p. 054018, arXiv: [1005.4451 \[hep-ph\]](#).
- [22] T. Plehn and M. Rauch, “Quartic Higgs coupling at hadron colliders”, *Phys. Rev. D* 72 (5 Sept. 2005) p. 053008, URL: <http://link.aps.org/doi/10.1103/PhysRevD.72.053008>.
- [23] J. Butterworth et al., “Single Boson and Diboson Production Cross Sections in pp Collisions at sqrt(s)=7 TeV”, tech. rep. ATL-COM-PHYS-2010-695, CERN, Aug. 2010.
- [24] S. Dittmaier et al., “Charged-Higgs-boson production at the LHC: NLO supersymmetric QCD corrections”, *Phys.Rev.* D83 (2011) p. 055005, arXiv: [0906.2648 \[hep-ph\]](#).
- [25] The ATLAS Collaboration, “Calibration of the b-tagging efficiency for c jets with the ATLAS detector using events with a W boson produced in association with a single c quark”, tech. rep. ATLAS-COM-CONF-2013-146, 2013.
- [26] G. Cowan et al., “Asymptotic formulae for likelihood-based tests of new physics”, *European Physical Journal C* 71 (Feb. 2011) p. 1554, arXiv: [1007.1727 \[physics.data-an\]](#).
- [27] A. L. Read, “Presentation of search results: the CL s technique”, *Journal of Physics G: Nuclear and Particle Physics* 28.10 (2002) p. 2693, URL: <http://stacks.iop.org/0954-3899/28/i=10/a=313>.

Acknowledgements

I would like to thank Prof. Markus Schumacher for providing me with the opportunity to gain an insight on modern particle physics in the course of this project.

I enjoyed my time as part of Prof. Schumachers group immensely due to the pleasant atmosphere and friendly colleagues. Regardless of my short time here, i always felt welcome and appreciated which means a great deal to me.

My special thanks goes out to Dr. Michael Böhler and Dr. Holger von Radziewski for their relentless support concerning technical and physics related issues as well as their invaluable proof-reading of various versions of this thesis.

I would also like to thank my friends, my family and my girlfriend for providing help, a hot meal or just lending an ear to my worries whenever needed.